Complex fault geometry and rupture dynamics of the M_w 6.5, 2016, October 30th central Italy earthquake

L. Scognamiglio[1], E. Tinti[1], E. Casarotti[1], S. Pucci[1], F. Villani[1], M. Cocco[1], F. Magnoni[1], A. Michelini[1] and D. Dreger[2].

[1]Istituto Nazionale di Geofisica e Vulcanologia, Via di Vigna Murata 605, 00143 Rome, Italy; [2]Berkeley Seismological Laboratory, University of California, Berkeley, California, USA.

Corresponding author: Laura Scognamiglio (laura.scognamiglio@ingv.it)

Key Points:

- **Rupture history of the October 30th 2016 Norcia earthquake is modeled by jointly inverting seismograms and GPS coseismic data**
- **Two main slip patches, with similar slip value and rupture times, occur up-dip from the nucleation on two differently oriented fault**
- **This result has implications for dynamic control of segmented fault systems in the Central Apennines due to geological structures inherited from past tectonics**

Abstract

We study the October 30th 2016 Norcia earthquake (M_W 6.5) to retrieve the rupture history by jointly inverting seismograms and coseismic GPS displacements obtained by dense local networks. The adopted fault geometry consists of a main normal fault striking N155°and dipping 47° belonging to the Mt. Vettore-Mt. Bove fault system (VBFS) and a secondary fault plane striking N210° and dipping 36° to the NW. The coseismic rupture initiated on the VBFS and propagated with similar rupture velocity on both fault planes. Up-dip from the nucleation point, two main slip patches have been imaged on these fault segments, both characterized by similar peak-slip values (~3 m) and rupture times (~3 s). After the breakage of the two main slip patches, coseismic rupture further propagated southeastward along the VBFS, rupturing again the same fault portion that slipped during the August 24th earthquake. The retrieved coseismic slip distribution is consistent with the observed surface breakages and the deformation pattern inferred from InSAR measurements.

Our results show that three different fault systems were activated during the October 30th earthquake. The composite rupture model inferred in this study provides evidences that also a deep portion of the NNE-trending section of the Olevano-Antrodoco-Sibillini (OAS) thrust broke co-seismically, implying the kinematic inversion of a thrust ramp. The obtained rupture history indicates that, in this sector of the Apennines, compressional structures inherited from past tectonics can alternatively segment boundaries of NW-trending active normal faults or break co-seismically during moderate-to-large magnitude earthquakes.

1. Introduction

There exists an extensive literature emphasizing the complexity of the rupture process during individual earthquakes and the role of rheological and frictional heterogeneities in controlling dynamic rupture propagation and the final slip distribution on the fault plane [Boatwright & Cocco, 1996; Johnson et al., 2006; Noda & Lapusta, 2013; Kaneko et al. 2010; among many others]. Earthquake source complexity is generally associated with the heterogeneity of the dynamic rupture parameters (slip velocity, slip duration, rupture velocity, final or maximum slip) on the assumed fault plane, usually inferred through kinematic inversions of geophysical data. It is also well known that geometrical complexities of the fault systems contribute to the heterogeneity of the dynamic rupture process [Harris & Day, 1999; Eberhart-Phillips et al., 2003; Wesnousky, 2008]. In this state of knowledge, recent earthquakes have shed light on

complex multi-fault ruptures during a single seismic event, pointing out the implications on seismic hazard assessment and the maximum expected magnitude in a given tectonically active area [see Fletcher et al., 2016; Beavan et al., 2012]. The 2016 M_W 7.8 Kaikoura earthquake (New Zealand) certainly represents the most interesting recent example of a multi-fault rupture, propagating on both mapped and unmapped fault segments, which raises serious concerns on our understanding of fault segmentation and dynamic ruptures on non-planar faults [Hamling et al., 2017].

The Apennines (Italy) have been struck by several seismic sequences in recent years, showing evidence of the activation of multiple segments of normal fault systems in a variable and relatively short time spans, as in the case of the 1980 Irpinia earthquake [three shocks in 40 s; Bernard & Zollo, 1989; Pantosti & Valensise, 1990], the 1997 Umbria-Marche sequence [four main shocks in 18 days, Chiaraluce et al., 2003] and the 2009 L'Aquila earthquake [three segments activated during the foreshock, mainshock and aftershock sequences within a few weeks, Valoroso et al., 2013]. Among them, the Central and Northern Apennines seismic sequences are typically characterized by the occurrence of repeated events with similar moderate-to-large magnitudes ($5.0 < M_W < 6.5$) and significant complexity during individual main shocks. In particular, earthquake ruptures display heterogeneous slip distributions on the causative fault system generated by both fault geometry and heterogeneous frictional properties [such as for the 2009 L'Aquila earthquake, Cirella et al., 2012]. Moreover, the coseismic activation of multiple segments can be influenced by pre-existing, inherited tectonic structures whose variable kinematic behavior may play a significant role in accommodating the present-day extensional regional tectonic setting [Chiaraluce et al., 2005; Pizzi & Galadini, 2009].

The Amatrice-Visso-Norcia 2016-2017 seismic sequence began on August 24th with a M_W 6.0 earthquake, which struck the region between Amatrice, Accumoli and Norcia (see Figure 1), and caused 299 fatalities and extensive damages in the urban and rural surrounding areas. Nearly two months after the beginning of the sequence another M_W 5.9 earthquake occurred on October 26th 2016 near Visso and Ussita at the northern edge of the aftershock zone of the August 24th event (see Figure1 and the map in Figure 2), extending the activated seismogenic area towards north-west. Four days after this "second main shock", on October 30th 2016, a third larger earthquake, M_W 6.5, occurred near Norcia, roughly midway between Accumoli and Visso (see Figure 1), severely damaging the already affected towns and villages in this sector of the Apennines. The October 30th main shock was preceded by almost sixteen

thousand aftershocks (M ≥ 1.5). The intense seismic activity that followed the initial main shock of August 24th prompted the evacuation of population from their houses and working environments and, although the October 30th event is the strongest earthquake in Italy since the 1980 Irpinia shock, no casualties were reported. The earthquake, however, further damaged Norcia and the surrounding towns and led to the collapse of numerous historical buildings of high cultural value.

The largest historical earthquake that struck the area occurred in 1703 near Norcia, it consisted of two shocks that occurred on January 14th (M_W 6.8) and February 2nd (M_W 6.7) [Rovida et al., 2016]. The historical event closest to the epicentral area is the 1639 earthquake [M_W 6.2, *CPTI2015*], which heavily damaged the town of Amatrice [Galli et al., 2016]. Seismicity in this region is characterized by normal-faulting earthquakes with rupture planes oriented nearly NW-SE, parallel to the Apennines' axis. Locations, depths and normal faulting mechanisms of the largest earthquakes of the 2016-2017 Amatrice-Visso-Norcia sequence indicate that ruptures originated in the shallow crust, where the current extensional regime overprints compressional structures and pre-orogenic faults, giving rise to a complex network of active faults. Overall, structural complexity plays a major role in the segmentation of normal faults and their interactions in this region [Gupta & Scholz, 2000; Nicol et al., 2006], with important consequences on seismic behavior and mechanics of earthquake faulting. This complexity is particularly evident in our study area and is corroborated by the coexistence of different fault plane solutions of nearby aftershocks [e.g., http://cnt.rm.ingv.it/tdmt; Scognamiglio et al., 2016; Chiaraluce et al., 2017].

The 2016 seismic sequence allowed for the collection of outstanding data-sets that include broadband and strong motion data, GNSS and high frequency GNSS (High-Rate GPS), satellite data and InSAR interferograms, coseismic surface breakages and deformation patterns, earthquake location catalogues and moment tensors. Several of these data have been used in near real-time by INGV scientists to interpret the evolution of seismicity and provide authoritative, expert opinions while reporting to the Italian Civil Protection for emergency management [Gruppo di Lavoro INGV sul Terremoto in centro Italia, 2017].

In this paper, we study the October 30th 2016 Norcia earthquake in order to retrieve the source model of this seismic event and interpret the rupture process in the framework of this complex sequence of moderate-to-strong magnitude earthquakes. We note that our preliminary attempts to model the slip distribution of the October 30th main shock using a single fault plane oriented along the Apennines did not provide convincing fits to the all of

the observed waveforms [Chiaraluce et al., 2017]. In addition, the deformation pattern inferred from satellite observations [see Figure 1-c; Cheloni et al., 2017] suggests the activation of a multi-fault structure, coherently with the complexity, length and width of the observed surface faulting within the Castelluccio basin. We investigate the role of multi-fault ruptures with the final aim of providing a robust scientific interpretation to the occurrence of the largest earthquake at the end of the sequence in-between the previous two main events.

2.   **Tectonic setting and geological observations**

The study area is located in the axial portion of the Umbria-Marche Apennines, a Neogene mountain belt composed of a multi-layer of Triassic-early Jurassic shallow-water and late Jurassic-Oligocene pelagic carbonates overlain by Miocene foredeep siliciclastic deposits [see Carminati & Doglioni, 2012, for a review] (Figure 1a). The area testifies the occurrence of multi-phased contractional and extensional deformation, which can be subdivided into three main tectonic phases: (1) pre-orogenic Jurassic extension was responsible for the fragmentation of the regional carbonate platform of the Adria domain (i.e. southern Tethys margin) in deep pelagic basins and relatively shallow-water structural highs corresponding to the Umbria-Marche slope/basinal domain to the north, and Latium-Abruzzi platform/margin domain to the south, separated by major tectonic structures [Ciarapica & Passeri, 2002; Butler et al., 2006]; (2) late Miocene-early Pliocene NE-verging compression generated the Umbria-Marche fold-and-thrust belt [e.g. Barchi et al., 1998a; Vezzani et al., 2010]; (3) post-orogenic, late Pliocene-Quaternary extension dissected the axial zone of the belt, controlling normal-fault bounded intramontane continental basins, and is responsible for the present-day seismogenic activity in the area [Lavecchia et al., 1994; Barchi et al., 1998b; Cavinato & De Celles, 1999]. Miocene-Pliocene thrusting and Quaternary normal faulting, accompanied by large-scale uplift [D'Agostino et al., 2001], contributed to build the rugged and elevated topography of the area (up to ca. 2500 m a.s.l.) with relief locally exceeding 1000 m (Figure 1a).

A major regional tectonic structure of the compressional phase is the Olevano-Antrodoco-Sibillini thrust (hereinafter, OAS) [Lavecchia, 1985; Centamore et al., 2009]: it forms a first-order orogenic arc of the Central-Northern Apennines, juxtaposing the antiformal Meso-Cenozoic carbonatic multi-layer over a wide Miocene foredeep basin that underwent about 10 km shortening [Bigi et al., 2011; Pierantoni et al., 2013, and references therein]. The OAS thrust displays a markedly curved shape in map view (Figure 1): N- to NNW-trending in the

northern part, and NNE-trending in the southern part where it separates the Umbria-Marche domain from the Latium-Abruzzi domain. In particular, the portion that outcrops to the south of the Sibillini Mts. was interpreted as a transpressive thrust ramp resulting from tectonic inversion of a NNE-SSW Jurassic normal fault system [i.e., the pre-orogenic Ancona-Anzio fault; Castellarin et al., 1978; Calamita et al., 2012a, and references therein; Di Domenica et al., 2014]. This segment of the OAS shows a complex geometry: it is characterized by parallel splays defining a compound fault zone, up to 1 km wide; it presents fault-bend folding structural style, with hanging-wall ramp on footwall ramp relationships [Calamita et al., 2012b].

Post-orogenic Quaternary extension, which according to geodetic measurements is in the 1.5-3 mm/yr range [Serpelloni et al., 2005, D'Agostino et al., 2009], is driven by nearly horizontal, NE-trending deviatoric stress, as documented by instrumental seismicity [Chiarabba et al., 2005], structural geology [e.g. Lavecchia et al., 1994] and *in situ* stress measurements [Montone & Mariucci, 2016]. These tectonics is mainly accommodated by SW-dipping, NW-SE trending normal faulting [e.g. Boncio et al., 2004a] but, in some cases, it is capable of reactivating favorably oriented older normal faults and inverted thrusts [Tavarnelli, 1999] or pre-existing cross-structures [Chiaraluce et al., 2005; Di Domenica et al., 2014; Pizzi and Galadini, 2009].

The eastern normal fault system affecting the axial portion of the Apennines includes SW-dipping master faults whose long-term activity controlled prominent tectonic depressions [e.g. Coltorti & Farabollini, 1995]. Several of these faults display clear geological and paleoseismological evidence of Quaternary activity and are invoked as responsible of many complex seismic sequences with moderate-to-large magnitude events occurred in historical and instrumental times [Galadini & Galli, 2003; Galli et al., 2008].

The most important extensional faults-systems of the Amatrice-Norcia area are the Mt. Vettore-Mt. Bove, north of the NNE-trending segment of OAS, and the Laga Mts. faults-systems, south of the OAS (hereinafter, VBFS and LMFS, respectively) (Figure 1a). The ∼30 km-long VBFS is composed of several, NNW-SSE trending splays, both synthetic and antithetic, that bound the western side of the Sibillini Mts. range, affecting the stiff lower units of the Umbro-Marchean domain and exposing the Jurassic deposits at their footwall (Figure 1a). This fault-system was considered dormant [Galadini & Galli, 2003; Boncio et al., 2004a] because of: 1) evidence of Holocene activity provided by paleo-seismological investigations; 2) potential of large seismic events (M>6.5) as suggested by the length of its

surface trace; and 3) occurrence of few M<6 earthquakes (M_W 5.6, 1719; M_W 6.0, 1730; M_W 5.7, 1859) in the past two centuries [Galadini & Galli, 2000; Rovida et al., 2016]. The LMFS is composed of two main aligned NW-SE trending segments with evidence of Late Pleistocene-Holocene activity [Galadini & Messina, 2001; Galadini & Galli, 2003; Boncio et al., 2004b] that affect the weak Miocene Umbria-Marche units [Bigi et al., 2009]. Conversely to the VBFS, this fault system experienced a moderate-magnitude seismic sequence in 1619-1672 [Rovida et al., 2016]. The VBFS and LMFS are not considered the sources of the largest mainshocks that struck the area in 1703 (January 14th, M_W 6.8, and February 2nd, M_W 6.7), since their macroseismic fields extend more to the west, close to Norcia and L'Aquila, respectively [Tondi, 2000].

Despite their internal geometric/structural complexities, the VBFS and LMFS were considered seismogenic sources substantially continuous down to seismogenic depth, and separated by an underlapping en échelon stepover, located in coincidence of the OAS, which could be assumed to be a barrier to coseismic rupture propagations [Boncio et al., 2004a; Pizzi & Galadini, 2009] According to Pizzi et al.[2017] the Amatrice-Visso-Norcia 2016-2017 seismic sequence support the hypothesis that a young splay of the VBFS have started to cut through the barrier, acting as a soft-linkage with the LMFS.

3.   The aftershock sequence

The analysis of the aftershock pattern reveals several important features corroborating the activation of multiple fault segments. Chiaraluce et al. [2017] analyzed the spatio-temporal evolution of seismicity from January 1st to November 29th 2016 for a total of nearly 26,000 earthquakes. The earthquakes appear to align predominantly along SW-dipping fault structures, although seismicity occurring on NE-dipping antithetic planes and other differently oriented structures became evident very early in the sequence. These authors emphasized that the normal fault system activated during the sequence of main shocks is bounded at depth (~8-10 km) by an east- and gently-dipping, 2-3 km thick band of seismicity characterized by the occurrence of microseismicity and small-magnitude extensional aftershocks (up to $M_W \sim 4.0$). This band represents the base of the seismogenic layer and possibly the decoupling between the upper and the lower crust. Chiaraluce et al. [2017] also corroborated the evidence that all the main shocks nucleated at the base of the normal fault system, which is therefore limited at depth by this east-dipping layer. They also confirmed that the first main shock of August 24th 2016 (M_W 6.0) was not preceded by foreshocks.

Figure 2 shows the distribution of 25,600 aftershocks relocated by Chiaraluce et al. [2017] that occurred between August 24th and November 29th 2016, which allows the identification of the nearly 60 km-long sector of the Apennine seismogenic belt activated by the three main shocks of August 24th, October 26th and 30th 2016. The seismogenic volume increased further toward SE in January 2017, when four moderate-magnitude earthquakes ($5.0 \leq M_W \leq 5.5$) occurred south of Amatrice in the Campotosto area along the LMFS. This made the total length of the activated seismogenic area parallel to the Apennine axis nearly 70 km. Figure 2 displays a map view of the seismogenic zone (Figure 2a) and two cross-sections, namely a SW-NE cross-section (N65°) perpendicular to the VBFS fault system (Figure 2b) and a NW-SE cross-section (N155°) longitudinal to the seismogenic volume (Figure 2c). Color-coded hypocenters shown in map and cross sections allow us to evidence the timing of the seismicity. These sections contain all earthquakes that occurred within 1.5 km from the vertical selected plane and are 30 km and 60 km long respectively. The August 24th and October 30th main shocks (light-grey and red stars, respectively) nucleated at the base of the seismogenic layer and all the aftershocks are quite shallow (< 10 km).

The August 24th M_W 6.0 mainshock nucleated below Accumoli town close to the intersection at the Earth's surface of the OAS with the VBFS to the NW and the LMFS to the SE (Figure 1). The coseismic slip during this earthquake is distributed along two mapped segments (see Figure 1b): the Amatrice segment of the LMFS to the SE and the Vettore segment of the VBFS between Accumoli and Norcia to the NW [Tinti et al., 2016; Figure 1a and b]. The aftershocks of this first main event show a good agreement with the slip distribution [Chiaraluce et al., 2017; Pizzi et al., 2017], although they are mostly located between Accumoli and Norcia with very few earthquakes along the Amatrice segment of the rupture zone. The August 24th M_W 6.0 earthquake caused ~5.0 km-long, extensional coseismic ground breaks with centimetric displacement [Emergeo Working Group, 2016; Pucci et al., 2017] along the southern section of the VBFS. No surface breakages were mapped on the Amatrice segment, despite the shallow depth of this slip patch and the relatively high peak slip value [Tinti et al., 2016; Pizzi et al., 2017].

The October 26th 2016 (M_W 5.9) mainshock nucleated near Visso and ruptured the north-western segment of the VBFS. Chiaraluce et al. [2017] reported that this earthquake is actually a double event likely rupturing two fault patches on the VBFS or two adjacent segments of the same fault system (see Figure 1b and dark-grey stars in Figure 2). The aftershocks' pattern in this northern section of the seismogenic volume is coherent with the

activation of the SW-dipping segment of the VBFS. In contrast, the aftershocks in the sector between Norcia and Accumoli shows a complex pattern with seismicity spread over a wide area perpendicular to the VBFS, suggesting the presence of different seismogenic structures. The October 26th M_W 5.9 earthquake caused ~7.0 km-long, discontinuous extensional coseismic ground breaks with centimetric displacement [Pantosti and the Open EMERGEO Working Group, 2017] along the northern section of the VBFS.

The October 30th 2016 earthquake (M_W 6.5) nucleated below Norcia along the VBFS, just above the aforementioned gently, E-dipping base of the seismogenic layer. The N65°E cross-section (A-A' in Figure 2b) displays an alignment of hypocenters revealing the SW-dipping segment of the VBFS that ruptured during the October 30th event, matching the main shock hypocenter and the position of surface ruptures on the Mt. Vettore segment [Pantosti and the Open EMERGEO Working Group, 2017]. The dip angle of this fault is nearly 50°, in agreement with the TDMT moment tensor solution. However, the same cross section shows seismicity both in the hanging-wall and in the footwall of this fault segment, corroborating the presence of multiple faults, belonging to different systems activated during the seismic sequence. The October 30th main shock produced coseismic surface ruptures extending for more than 25 km along several strands of the VBFS (light violet stripe in Figure 1a). The width of the overall near-fault coseismic deformation zone reaches a maximum of ~2.5 km in the central part (near Castelluccio Plain), with throws locally exceeding 2 m [average value ~0.3 m; Pantosti and the Open EMERGEO Working Group, 2018]. Noteworthy, coseismic surface breakages have been observed again along the same southern section of the VBFS that ruptured during the August 24th earthquake.

The longitudinal section (B-B' in Figure 2c) provides a general view of the seismicity distribution along the northern portion of the LMFS and over the entire VBFS. This figure corroborates the observation that seismicity is associated with the activation of the Amatrice segment of the LMFS and the VBFS north of Accumoli up to Pieve Torina, moreover it shows that aftershocks occur within the first 8-10 km of depth, just above the E-dipping seismicity layer [Chiaraluce et al., 2017]. Figure 2c also points out the complex distribution of seismicity between Visso and Accumoli, corresponding to the area where the coseismic rupture initiated during the October 30th (M_W 6.5) earthquake, and it depicts a NNW-dipping alignment below Castelluccio di Norcia, which points to the surface emergence of the southern, NW-dipping section of the OAS. Moreover, the presence of seismic activity on both normal faults antithetic to the SW-dipping VBFS and differently oriented faults,

possibly inherited from past tectonic episodes, is consistent with observations from SAR interferometry [Cheloni et al., 2017] and the heterogeneity of fault plane solutions in the area. In particular, there are focal mechanisms consistent with the rupture of a ～N210° trending fault, with W- to NNW-dipping nodal planes (see Supplementary Material, S1) [Scognamiglio et al., 2009; Scognamiglio et al., 2010], likely associated with a portion of the OAS (http://cnt.rm.ingv.it/tdmt).

The far-field coseismic crustal deformation detected by Alos2 interferograms [Cheloni et al., 2017] after the M_W 6.5 earthquake shows a distribution of the fringes characterizing a maximum gradient of the displacement field along the VBFS (see Figure 1c). Moreover, southwest of the intersection between the OAS and the VBFS at Arquata del Tronto (see Figure 1a, c), the fringes' pattern also evidences a high gradient of displacement and a sharp change in the direction coherently oriented with the NNE-trending, SW-dipping OAS section. Finally, another prominent feature of the fringes' pattern is the extension of the subsidence zone and the uplift in the Norcia area, which is difficult to interpret as being generated exclusively by the coseismic slip on a single SW-dipping normal fault, thus suggesting the contribution of different fault segments in the rupture of the 30th October main shock [Cheloni et al., 2017].

Another aspect of attention is the unusual non-double-couple component (CLVD) observed for the TDMT solution of the 30th October main shock [see Figures 1 and 2; http://cnt.rm.ingv.it/tdmt, Scognamiglio et al., 2016; Chiaraluce et al., 2017]. This is quite surprising for moderate-to-large magnitude earthquakes in the Apennines, which are usually characterized by very high (≥ 90%) double-couple normal-faulting solutions oriented parallel to the Apennines axis. Although we are aware that the amount of CLVD in moment tensors calculations could be depth dependent, this observation might be interpreted as an evidence for a non-planar fault geometry and complex slip behavior during the October 30th main shock.

4. **Inverted Data**

To retrieve the coseismic rupture history of the October 30th earthquake, we jointly inverted the accelerograms recorded by permanent and temporary seismic stations and the coseismic displacements obtained by GPS data collected by continuous and campaign observations. The large number of temporary stations installed after the first main shock at the end of August

insured acquisition of an excellent data set in terms of near fault recordings and station azimuthal coverage and density (Figure 3).

4.1 Strong motion waveforms

We inverted the strong motion recordings of 36 three-component, digital accelerometers belonging to the National Accelerometric Network (Rete Accelerometrica Nazionale, RAN, http://ran.protezionecivile.it/IT/index.php) of the Italian Department of Civil Protection, and to the National Seismic Network (Rete Sismica Nazionale, RSN) of INGV [Michelini et al., 2016; Moretti et al., 2016]. These stations were all located within 45 km from the epicenter (Figure 3). The recorded accelerograms were processed to remove the instrument response, band-pass filtered between 0.02 and 0.5 Hz using low-pass and high-pass filters with two poles and two passes (zero-phase filtering), and finally time-integrated to obtain ground velocity time histories. Recorded and synthetic seismograms are filtered in the same way. The maximum frequency of 0.5 Hz was selected in order to significantly reduce the potential contributions of local site effects [Bindi et al., 2011; Cultrera et al., 2016] into the source modeling. Finally, the processed time histories were resampled at 10 samples per second.

4.2 GPS data.

We inverted the coseismic displacements of 105 three-component, continuous and campaign GPS stations downloaded from the RING web-site (http://ring.gm.ingv.it) (Figure 3). The stations belong to three geodetic networks: INGV-RING [Avallone et al., 2010], INGV CaGeoNet [Galvani et al., 2012] and Istituto Geografico Militare network (IGM, http://www.igmi.org). We selected all sites necessary to guarantee a good azimuthal coverage. The released data were previously processed by the three INGV GPS data analysis centers. Specifically, these centers used three different analysis softwares (GAMIT/GLOBK, GIPSY and BERNESE) to process observations [Avallone et al., 2010], and later combined the results into a single, consensual, co-seismic solution, to minimize potential systematic errors present in the individual solutions. The resulting largest horizontal coseismic displacements were obtained at stations VETT and MSAN, being 38.3 cm toward north-east and 26 cm toward south-west, respectively. The largest vertical offsets were obtained for stations ARQT, RIF and MSAN, with a subsidences of ~45, ~26 and ~17 cm, respectively [INGV Working Group "GPS Geodesy, GPS data and data analysis center", 2016].

5. Methodology and model parameterization

5.1 Inversion Methodology

The inversion code consists of a non-negative, least squares inversion method with simultaneous smoothing and damping [Hartzell & Heaton, 1983; Kaverina et al., 2002; Huang et al., 2013; Dreger et al., 2005]. The method allows the simultaneous inversion of seismic waveforms and geodetic data to retrieve slip amplitude and direction on an extended fault parameterized in terms of equal-area sub-faults.

This approach assumes a constant rupture velocity and allows the use of multiple time windows to account for potential variations in rupture propagation and local rise time. In each time window the source-time function is a boxcar function, representing slip velocity, having a given constant rise-time. Moreover, when two or more faults are considered, the procedure requires the assumption of a "hypocenter" (i.e., rupture initiation point) for each fault plane. This implies that the relative location where rupture starts on successive faults as well as the delay times with respect to the earthquake origin time (coseismic rupture onset) have to be assigned a priori.

The values of slip duration and rupture velocity as well as the local position of the rupture initiation point and the temporal delay of rupture propagation on a successive fault plane are thus selected iteratively by performing inversions with different values of these parameters and by quantitatively measuring the fit based on a variance reduction, as defined in Dreger et al. [2005].

5.2 Crustal Model

In order to model the strong motion waveforms, the Green's functions are computed using a frequency-wavenumber integration code [Saikia, 1994; Wang & Herrmann, 1980], while the static displacement Green's functions for inverting geodetic data are computed using the EDGRN/EDCMP codes [Wang et al., 2003]. The latter allows the calculation of Green's functions in a 1D layered elastic model.

The Green's functions for modeling both seismological and geodetic data have been computed by adopting the same crustal structure, CIA model (Central Italian Apennines), proposed for Central Apennines by Herrmann et al. [2011]. The detailed description of this model is provided in the Supplementary Material (S2) [Di Luzio et al., 2009; Herrmann et al., 2011]. The Green's functions for seismic waveforms were computed on a regular grid

sampling the focal volume every 1 km horizontally and 1 km vertically and filtered between 0.02 and 0.5 Hz (the same as for the recorded data).

5.3 Constraining fault geometry

The fault geometry selected in this study to perform the inversion of ground velocity time histories and GPS coseismic displacements consists of two faults: a main fault oriented along the Apennines belonging to the VBFS striking N155° and dipping 47° to the SW and a second fault plane striking N210° and dipping 36° to the NW. In our interpretation, the latter corresponds to the deep portion of the OAS, as we will further discuss in the followings. We didn't need to perform a through exploration of the main fault geometry since the surface trace of the VBFS is mapped in great detail, moreover plenty of evidence puts further constraints on the seismogenic fault plane, in particular: (i) the direction of the fringes' gradient inferred by SAR interferograms hinting the fault strike, (ii) the location of the main shock hypocenter, (iii) the location of the observed fault surface breakages and (iv) the moment tensor solution. Moreover, the geometry of the main fault adopted in this study for the VBFS segment is very similar to that proposed by Cheloni et al. [2017] and Pizzi et al. [2017].

As evidenced in the previous sections, the need for a secondary fault plane is strongly suggested by the observed deformation pattern inferred from the geodetic observations [Cheloni et al., 2017], in particular SAR interferograms. Moreover, the aftershocks distribution in the area between Accumoli and Norcia, the inferred non-double-couple component of the main-shock moment tensor and the existence of a non-negligible number of NE-SW trending focal mechanisms in the VBFS hanging-wall (see Supplementary Material, S1) provide other evidence supporting this interpretation. The selected fault geometry is coherent with the tectonic setting and the surface expressions of the known mapped faults.

The length of the modeled main normal fault is 34 km and the downdip width is 16 km, while the secondary fault is 10 km long and 14 km wide. The shallow top borders of these faults are located at 0.012 km and 1.8 km below the modeled free surface, respectively. Taking into account the elevation of the inverted stations, the model datum is ~850 m a.s.l..

Despite the relevant observational constraints cited above, the optimal geometry of the secondary fault has been inferred through a grid search approach according to the following strategy: a) while keeping fixed the geometry of the VBFS plane, we test different geometries

for the secondary fault by running different single-window inversions and checking the misfit reduction of the strong motion data; b) subsequently once the geometry of the best fitting model is identified, we run a multi-window inversion of both the strong motion and GPS coseismic displacements; c) finally, we analyze the model space (slip amplitude and direction, rupture velocity) of the inverted rupture histories to check the stability of the inferred kinematic parameters. Geological information was used to explore the different combinations of strike and dip angles of the secondary fault: strike angle varied between 180° and 250°, while the dip angle varied between 10° and 60° both in steps of 10°. We also varied the position of the intersection of the secondary fault relative to the main normal fault. While constraining the fault geometries, we let the kinematic parameters vary coarsely in a broad range consistent with the values previously explored for the main events of this sequence [Tinti et al., 2016, and Chiaraluce et al., 2017].

5.4 Fault parameterization

Once the fault geometry was selected, we ran the joint inversion of strong motion and GPS data by using the multi-window approach and searching for slip distribution, rise time, rupture velocity on both fault planes, and for delay time and relative hypocenter location on the second fault. We use the INGV hypocenter located at 42.84°N, 13.11°E at a depth of 9.52 km (http://cnt.rm.ingv.it/event/8863681) to place the rupture onset on the VBFS fault plane. Both fault planes are parameterized using sub-faults having a 2×2 km² area.

We allowed rise time of each time window and rupture velocity of both fault planes to range between 0.5 and 1.5 s, and 2.5 and 3.0 km/s, in steps of 0.1, respectively. We assumed three time windows separated by rise time duration. The rake on the N155° fault was allowed to be heterogeneous throughout the fault and ranging between 45° and 125°, that is ±45° with respect to a pure normal slip mechanism. In contrast, on the second N210° fault, the rake was allowed to range between 10° and 100° to account also for strike-slip components of motion.

The allowed delay time for the rupture onset on the second fault ranges between 0.0 s and 2.0 s, in steps of 0.2 s. The location of the starting rupture on the second fault was allowed to lie on the deeper 5 sub-faults edging the main fault. To reach the final rupture history of the 30th October event, we explored almost 22000 models: 330 runs were performed exclusively to investigate the relative location and starting time of the second nucleation point and the rupture velocity on the second fault because of the potential trade-off among these parameters

(see Supplementary Material, S3).

6. **Results**

Figure 4 shows the best-fitting source model retrieved from the simultaneous inversion of strong motion waveforms and GPS coseismic displacements. The retrieved values of the kinematic parameters are listed in Table 1. The two datasets have an equal weight and the amount of smoothing (regularization) is adjusted to trade-off with data variance reduction and model smoothness.

The best-fitting kinematic rupture model imaged through the multi-window approach shows the following main features: i) coseismic rupture initiated on the N155° fault (VBFS) and after ~1s propagated with similar rupture velocities on the two fault planes (N155° and N210°); ii) main slip patches are located up-dip from the nucleation point and are characterized by a similar peak slip value of ~3 m; iii) peak slip values are simultaneously reached on both faults between 3 and 4 s after the rupture onset (see Figure 4); iv) shallow slip patches on the main N155° fault are consistent with the observed surface faulting; and v) variable rake angle with clear differences between the two faults; vi) coseismic rupture further propagated southward along the N155° normal fault (VBFS) after the breakage of the two main slip patches. Specifically, the rake angle on the main N155° fault is almost pure dip-slip, whereas on the second N210° fault the rupture starts with a significant left-lateral strike-slip component (rake ~ 20°) on the main slip patch and rotates to an almost pure normal motion toward the south-western edge of the fault. To this regard, we note that the slip direction on the main slip patch along the N210° secondary fault (rake ~ 20°) is kinematically compatible with the orientation of the present-day extensional tectonic setting. Figure 5 shows the snapshots of slip velocity distribution with time emphasizing the details of rupture propagation on both fault planes adopted in this study.

Figures 6 and 7 show the comparison between the synthetic ground velocities with the observed strong motion waveforms and between the calculated coseismic displacements and GPS data, respectively. The fit to recorded seismograms is remarkably good, the arrival times and amplitudes for the majority of recorded time histories at all stations and azimuths are well reproduced with a total variance reduction (VR) of 75.92%. The fit of the closest stations in many cases exceeds 80% of VR (e.g. CLO, T1214, ACC, CNE). The synthetic GPS vectors fit well magnitudes and directions of the observed horizontal and vertical displacements resulting in a fit with VR=99.57%. The final model VR of the presented

kinematic model is 76.05%. Further details on the ensemble of rupture models providing a very good fit to the data as well as on the identification of the best-fitting model are provided in the Supplementary Material (S3).

The total inferred seismic moment is 8.8e+18 Nm (M_w=6.56), partitioned into 5.9e+18 Nm (M_w=6.45) on the main fault and 2.9e+18 Nm (M_w=6.25) on the second fault.

It is worth mentioning that the fit to the observed strong motion and GPS data obtained with the abovementioned two faults model is much better than that retrieved from other inversion attempts using a single normal fault striking N155° (see Supplementary Material, S3). In particular, the model presented in this study allows the fit to the recording sites closest to the nucleation or located to the South-East (such as NRC, T1213, CSC, T1214, ACC, AMT; see Figure 3), which were not well modeled in the first fast-inversion performed using the single fault model described by Chiaraluce et al. [2017].

7.   Forward model of InSAR Data

The two-faults rupture model proposed in this study differs from the two alternative models proposed by Cheloni et al. [2017]. These authors inverted GPS and SAR interferograms to determine the slip distribution of the October 30th earthquake. They proposed for this main shock two alternative source models both consisting of two faults: the two models differ for the geometry of the secondary fault, having the first coinciding with the Mt. Vettore-Mt. Bove fault system (corresponding to VBFS in our study). The authors considered the following geometries for the secondary fault: a NE dipping fault antithetic to the VBFS and a WNW-dipping low angle fault in the hanging wall of the VBFS. Although they concluded that the secondary fault is necessary to better reproduce the complex deformation pattern associated with the M_W 6.5 October 30th main shock, the inversion of geodetic data alone did not allow the identification of a unique best-fitting model. Furthermore, the WNW-dipping fault adopted by Cheloni et al. [2017 is different from the secondary fault of this study. To verify the capability of the geometry proposed by the Cheloni et al. [2017] of reproducing our data-set, we have tested their model by performing a series of joint inversions of strong motion and GPS data, where the N210° fault has been replaced by the antithetic one. We emphasize that, according to our inversion analysis, the fit to strong motion data, in particular those recorded at the stations located close to the hypocenter and to the S-SE, is significantly good only when we include the N210° fault in the model. Those stations allowed us to constrain the geometry of the secondary fault.

However, to further corroborate and cross-check our analysis we performed a forward modeling of InSAR measurements using the source model proposed in this study.

We modeled the satellite data acquired by the ascending and descending orbits along the line of sight of Advanced Land Observing Satellite-2 (Alos2) [Cheloni et al., 2017]. The time interval of the two Alos2 interferograms covers, however, both the October 26th and the October 30th mainshocks, and it does not allow to discriminate between the surface displacement effects produced by the two earthquakes separately in the northern region. Figure 8 shows the InSAR data (left panels), the synthetic deformation field computed with our kinematic rupture model including also the October 26th rupture as imaged by Chiaraluce et al. [2017] (mid-panels), and the residuals (right panels). Data and forward model are projected along the line of sight of Alos2-descending (top panels) and ascending (bottom panels) tracks.

We observe a remarkable similarity between the simulated deformation pattern using our best-fitting model and that obtained from the InSAR measurements. Our model is capable to reproduce the shape and the extension of the deformation, as well as the abrupt deformation gradient to the south, characterized by a NE-SW trend, and the shape and amplitude of the deformation lobe of Norcia. The residuals between synthetic and observed deformation patterns show that the discrepancies are located near the fault surface expression, which are likely due to along-strike geometrical complexities of the segments not included in our fault model, as well as to the effect of topography (not included in our simulations). Moreover, the residuals might also be related to the large temporal span between the two passages of the satellite, which includes several days and, in particular, the October 26th main shock. In any event, we can consider the calculated discrepancy more than satisfactory, considering that our model has been inferred without inverting InSAR measurements.

8. Discussion

Our interpretation of the rupture model inferred for the October 30th earthquake by inverting velocity converted strong motion waveforms and coseismic GPS displacements relies on the activation of two differently orientated faults: in particular, we modeled a N210° blind fault segment that we connect with the OAS at depth in addition to the SW dipping main fault (VBFS). Therefore, it is relevant for the understanding of our results to discuss the evidence supporting this interpretation. To this task, we have elaborated two geological cross-sections, about 20 km-long, oriented orthogonal to the two fault segments modelled in this study (A-A'

and B-B', respectively; Figure 1). The sections were drawn by assuming a partial involvement of the Paleozoic basement units, as suggested by Lavecchia et al. [1988] and Calamita et al. [1991]. Dip-domains and thickness of the outcropping formations were derived by compiling existing 1:10,000 scale geological maps [Regione Umbria: http://geo.umbriaterritorio.it/umbriageo/atlante/; Regione Marche: http://www.ambiente.marche.it/Territorio/Cartografiaeinformazioniterritoriali; Centamore et al., 1992; Pierantoni et al., 2013], whereas we assigned to the lowermost units (Triassic to Early Jurassic formations, whose base does not crop out in the study area) a minimum 3 km total thickness, based on deep borehole data and regional correlations [see also: Bigi et al., 2009; Speranza and Minelli, 2014]. Although we assume a partial involvement of the Paleozoic basement units, as suggested by Lavecchia et al. [1988] and Calamita et al. [1991], due to the missing information on the deep structures (such those from seismic reflection profiles), the tectonic structures drawn beneath -2.0 km a.s.l. are speculative and detachments imbricating the Triassic formation (Evaporites) are possible.

Section A-A' (Figure 9) intersects the Norcia Quaternary basin and several splays of the VBFS, as well as the outermost splays of the N-trending section of the OAS. The structural style adopted in building this section is characterized by fault propagation folds according to Calamita et al. [2012b]. Here, the outcropping Meso-Cenozoic multi-layer was emplaced during the orogenic phase onto the Miocene siliciclastic units (i.e. Laga Fm.) through the leading shallow-dipping OAS. As a result, at its hanging-wall, the latter strongly uplifted the lower units of the Umbria-Marche multi-layer and, possibly, juxtaposed the Paleozoic basement onto the Meso-Cenozoic sequence. The later high-angle Quaternary normal faulting crosscuts the compressive structures: the most external extensional front is located on the backlimb of the Mt. Vettore fold and shows, along with the Norcia basin faults system, the largest long-term offset. From this reconstruction, the connection between the N155° modelled fault and the VBFS showing the coseismic surface ruptures is straightforward.

Section B-B' (Figure 10) is oriented N120° and orthogonal to the N210°-trending fault resulting from our best-fitting inversion. Here, the structural setting is characterized by a flat carbonate thrust-sheet displaying, at the hanging-wall block of the OAS, a narrow anticline verging to the SE with a small overturned forelimb and overthrusting the Miocene hemipelagic and foredeep flysch deposits (i.e. Laga Fm.). Here, also, the lower units of the multi-layer were strongly uplifted and, possibly, the Paleozoic basement was juxtaposed to the Meso-Cenozoic sequence. The structural style adopted in building this section is,

conversely, characterized by fault bend folding along the NNE-trending section of the OAS, according to Calamita et al. [2012b], with an outcropping shallow-dipping section. Worthy to note, adopting such structural style, the location and dip of the modeled N210°-trending fault appear to coincide with the blind ramp section of the ramp-flat geometry invoked for the OAS. Two main NW-trending faults are recognized close to Norcia town, whose shallow intersection with the OAS ramp can be ruled out. In the hanging-wall of the OAS thrust, few Quaternary NW-dipping normal faults bounding the Castelluccio Plain to the south were recognized and possibly can join the modeled N210°-trending fault at ~3 km of depth.

According to this reconstruction, we can hypothesize that the complex rupture process of the 30th October earthquake also involved a significant portion of the blind ramp of the NNE-trending OAS where it trends NNE. This interpretation implies a kinematic inversion of the Miocene transpressive thrust ramp, which on its turn already results from tectonic inversion of Jurassic normal faulting, thus confirming its role as weak crustal structure.

The coseismic rupture nucleated along the N155° fault (VBFS) in-between the August 24th and the October 26th main shocks, suggesting that the Mt. Vettore-Mt Bove fault system (VBFS) was loaded by: the stress perturbations caused by these two previous earthquakes, the remote tectonic strain and, likely, by the strain partitioning in the shallower crust. The last one caused by the decoupling represented by the shallow east-dipping layer [Chiaraluce et al., 2017] bounding at depth the seismogenic layer in this area. In agreement with Pizzi et al. [2017], the inferred rupture model displays a modest amount of slip in the vicinity of the nucleation area (see Figures 4 and 5), similarly to what imaged for the 2009 L'Aquila earthquake [Cirella et al., 2012]. The earthquake rupture quite suddenly (within 1.0-2.0 seconds) starts propagating also on the N210° fault segment (Figure 5) which, according to our interpretation, belongs to a deep portion of the NE-trending OAS section: this suggests that also this fault segment was loaded and characterized by a high pre-stress. During the first 4 seconds the coseismic rupture is propagating nearly up-dip on the VBFS and along-strike into the N210° fault segment reaching similar peak slip values (~3 m) on both faults. Thus, the two main slip patches on these two fault segments break simultaneously (after ~3 s), therefore jointly contributing to the radiated seismic waves and to the coseismic deformation pattern, including surface breakages.

The position of the shallow slip patches as well as the slip directions on the two fault segments belonging to the VBFS and OAS are consistent with the extensional setting and with the pattern of the observed surface breakages. However, it is important to emphasize that

the pattern of surface breakages parallel to the VBFS, and its width in the perpendicular direction (2.5-3 km), are the sole expression of coseismic slip at depth along two different fault segments belonging to two distinct fault systems. While the coseismic rupture along the N155° normal fault reaches the Earth's surface, the main slip patches on the N210° segment is deeper than 1.8 km. Wilkinson et al. [2017] reports novel records of near-fault coseismic displacements during the October 30th 2016 main shock obtained from low cost GNSS receivers located onto the portion of the VBFS that ruptured the surface. They provide instrumental evidence that large near-field displacements and surface breakages ceased within 6-8 seconds of the nucleation time, which is consistent with the rupture history proposed in this study. They conclude that the surface ruptures observed after this main shock are caused by the propagation of slip from depth on the rupturing fault array. Our results suggest that this fault array at depth is not limited to NW-SE normal faults of the VBFS.

The coseismic rupture after branching from the N155° fault and rupturing the N210° segment, propagated farther (between 4 and 8 seconds after the initiation) along the southern portion of the VBFS toward the southeast (see Figure 5), rupturing again the same fault segment that slipped during the August 24th 2016 main shock. Figure 11 shows the comparison between the slip distributions imaged on the VBFS fault during the August 24th [red contours; Tinti et al., 2016] and the October 30th 2016 main shocks (blue contours; this study). This figure points out that coseismic slip during the October 30th main shock along the southernmost portion of the VBFS and the Amatrice segment of the LMFS displays a slip patch located between the two asperities that ruptured during the August 24th event, just below Accumoli and Arquata del Tronto demonstrating continuity in the coseismic rupture propagation along and on the single fault plane that ruptured during the first main shock of the sequence. Moreover, the figure also shows that a relevant portion of the southern segment of the VBFS slipped both during the August 24th (M_W 6.0) and the October 30th (M_W 6.5), raising questions on the way the VBFS has released its seismogenic potential during the three main shocks of the 2016-2017 Amatrice-Visso-Norcia seismic sequence. It is important to emphasize that the coseismic rupture, rupturing twice the same slip patch at depth on the VBFS, is coherent with the geological observations of reoccurrence of surface breakages at the same location along the Mt. Vettore fault segment [Pantosti and the Open EMERGEO Working Group, 2017], keeping in mind that the two main slip patches characterizing the rupture history of the October 30th earthquake are located along a different portion of the N155° and along the N210° fault segments.

There are several explanations to justify the re-strengthening of an asperity shortly after its coseismic rupture, each one not necessarily excluding the others. A first explanation relies on the heterogeneous distribution of frictional properties (represented by constitutive dynamic parameters) on the fault plane and on considering the presence of a weak, velocity weakening [Boatwright & Cocco, 1996] patch unable to stop the propagating coseismic rupture. However, this explanation contradicts the rupture of the same patch like an asperity during the August 24th main shock [Tinti et al., 2016]. A second explanation relies on the pressurization of deep fluids [Rice, 2006; Bizzarri & Cocco, 2006a, 2006b; Rudnicki & Rice, 2006] causing the fast re-strengthening and the reloading of the fault patch, thus increasing prestress to a level that enables subsequent ruptures. However, we do not have so far observations suggesting the circulation of fluids in the fault zones during the 2016 sequence [differently from the 1997 Colfiorito and 2009 L'Aquila seismic sequences: Miller et al., 2004; Lucente et al, 2010; Di Stefano et al., 2011]. Moreover, it is unclear why fluid pressurization should be localized only in this fault portion. A third, more intriguing, explanation relies on coseismic normal stress changes [Perfettini et al., 1999, 2001] caused on this southern portion of the VBFS by the rupture of the N210° fault. This is a dynamic effect caused by the peculiar fault geometry and the coseismic rupture history. Indeed, during the first 4 seconds the slip on the main patches on the N155° and N210° fault segments can reduce the normal stress (unclamping) on the southern portion of the VBFS, thus favoring the propagation of the coseismic rupture in the patch that previously slipped during the August 24th shock. Finally, a fourth explanation is incomplete stress drop in the earlier events; sufficiently high residual shear stress might have maintained the conditions for a propagating rupture on the same fault area.

The composite source model proposed in this study to image the rupture history during the October 30th 2016 main shock reveals an extraordinary complexity, corroborated by several observations that are not limited to the inverted data. This complexity is not solely expressed by the number and the geometry of fault segments co-seismically activated. What was surprising is the simultaneous coseismic rupture of faults originated in different tectonic settings and characterized by very different orientation and geometry. The imaged rupture history indicates that, in this sector of the Apennines, compressional structures do not solely play a passive role as fossil structures that control the segmentation of the Quaternary normal faults NW-SE oriented, but they can even break co-seismically contributing to generate a M$_W$ 6.5 earthquake at the end of a prolonged seismic sequence.

9. Conclusion

The inversion of recorded ground-velocity waveforms and coseismic GPS displacements collected by a dense network of receivers has allowed us to constrain the fault geometry and to retrieve the rupture history of the October 30th (M_W 6.5) earthquake. Our results show that the coseismic rupture occurred on two fault segments: a N155° striking, SW-dipping fault and a secondary fault plane striking N210° and dipping 36° to the NW, the latter branching from the first one in proximity of the hypocenter. Coseismic slip is concentrated in two main patches located on both fault segments, reaching a peak value of nearly 3 meters three seconds after the nucleation at the hypocenter. The coseismic rupture further propagated toward the SE breaking again the northern patch of the August 24th earthquake. In addition, the imaged source model displays an additional slip patch (~1 m max slip) located in between the two coseismic slip concentrations imaged for the August 24th earthquake.

Three distinct fault systems, well-known by geologists, were activated during the seismic sequence, and they participated to the rupture history of the October 30th (Mw 6.5) main shock: the VBFS, the NNE-trending OAS segment and the northern tip of the LMFS (see Figures 1 and 2). The composite rupture model inferred in this study confirms that a secondary rupture plane is necessary to fit the collected data (see Supplementary Material, S3), which we have interpreted as a deep portion of the OAS. This secondary fault broke during the coseismic rupture, releasing a seismic moment corresponding to M_W 6.25 and suggesting a kinematic slip-reversal on a thrust ramp. We have also performed a forward modeling of InSAR observations demonstrating that the proposed multi-fault source model is consistent with the deformation pattern resulting from InSAR interferograms. These results have important implications for the interaction between segmented fault systems in the Central Apennines as well as for the role played by coseismic dynamic ruptures in activating geological structures inherited from past tectonics.

The rupture history during the October 30th main shock was also quite peculiar. Indeed, the simultaneous rupture of the two main slip patches on the two different fault segments (the N155° and the N210° faults) has important implications for the radiated seismic waveforms and for the observed pattern of surface breakages along the VBFS and within the Castelluccio Plain. This provides an interpretation of the unusual non-double couple component inferred from the moment tensor solution (TDMT), which is anomalous if compared with other moment tensor solutions in this sector of the Apennines during the present and past seismic sequences. Seismological observations suggest that the October 30th earthquake is a single

event that nucleated on the N155° normal fault belonging to the VBFS with coseismic rupture that propagated onto the N210° fault quite suddenly after its initiation on the main fault. The rupture history revealed a quite evident up-dip propagation with relevant rake rotations on the N210° fault plane. This might also have important implications for the interpretation of the observed rupture directivity and ground shaking during the October 30th main shock.

The spatio-temporal evolution of seismicity during this seismic sequence, and in particular the nucleation of the largest-magnitude earthquakes, suggests a relevant partitioning of the loading-rate on different fault segments belonging to different systems. The extensional tectonic stress loading a shallow seismogenic layer (~8-10 km), likely decoupled from the deeper crust and stress perturbations caused by previous earthquakes can explain the nucleation of the October 30th main shock in between the previous two main earthquakes on the VBFS as well as the increase of pre-stress on the N210° fault segment. Moreover, the subsequent simultaneous rupture of the N155° and N210° faults can have dynamically reduced the normal stress on the southeastern section of the VBFS, thus allowing the rupture to penetrate in the northern slip patch and in the nucleation area of the August 24th main shock. Modeling dynamic Coulomb stress changes is beyond the goal of the present work; we simply speculate in this study that several processes, including unclamping due to dynamic normal stress changes, can explain the coseismic rupture propagation on the same fault segment during two distinct main shocks.

Future investigations should address the details of the rupture history, such as the imaging of the variations of rupture velocity and of the peak slip values, to help unravelling the anatomy of these complex fault systems and of their tectonic coupling during both the interseismic and the coseismic phases of the seismic cycle. The results presented in this study can contribute to stimulate the scientific research in this direction to better understand fault segmentation and the dynamic control on the activation of fault segments during sequences of normal faulting earthquakes.

References

Avallone, A., G. Selvaggi, E. D'Anastasio, N. D'Agostino, G. Pietrantonio, F. Riguzzi, ... L. Zarrilli (2010). The RING network: improvement of a GPS velocity field in Central Mediterranean. *Annals of Geophysics, 53*(2).

Barchi, M., DeFeyter, A., Magnani, B., Minelli, G., Pialli, G., & Sotera, B. (1998a). The structural style of the Umbria-Marche fold and thrust belt. *Memorie della Societa Geologica Italiana, 52*, 557-578.

Barchi, M., DeFeyter, A., Magnani, M., Minelli, G., Pialli, G., & Sotera, B. (1998b). Extensional tectonics in the Northern Apennines (Italy): evidence from the CROP03 deep seismic reflection line. *Memorie della Societa Geologica Italiana, 52*, 528-538.

Beavan J., Motagh M., Fielding E. J., Donnelly N., & Collett D. (2012). Fault slip models of the 2010–2011 Canterbury, New Zealand, earthquakes from geodetic data and observations of postseismic ground deformation. *New Zealand Journal of Geology and Geophysics, 55*(3), 207-221.

Bernard, P., & Zollo, A. (1989). The Irpinia (Italy) 1980 earthquake: Detailed analysis of a complex normal faulting. *J. Geophys. Res., 94*(B2), 1631–1647. doi:10.1029/JB094iB02p01631.

Bigi, S., Milli, S., Corrado, S., Casero, P., Aldega, L., Botti, ... Cannata, D. (2009). Stratigraphy, structural setting and burial history of the Messinian Laga basin in the context of Apennine foreland basin system. *Journal of Mediterranean Earth Sciences*, *1*, 61-84.

Bigi, S., Casero, P., & Ciotoli, G. (2011). Seismic interpretation of the Laga basin; constraints on the structural setting and kinematics of the Central Apennines. *Journal of the Geological Society*, *168*(1), 179-190.

Bindi, D., L. Luzi, S. Parolai, D. Di Giacomo, & G. Monachesi (2011). Site effects observed in alluvial basins: The case of Norcia (Central Italy). *Bull. Earthquake Eng., 9*(6), 1941–1959. doi:10.1007/s10518-011-9273-3.

Bizzarri, A., & M. Cocco (2006a). A thermal pressurization model for the spontaneous dynamic rupture propagation on a three-dimensional fault: 1. Methodological approach. *J. Geophys. Res., 111*, B05303. doi:10.1029/2005JB003862.

Bizzarri, A., & M. Cocco (2006b). A thermal pressurization model for the spontaneous dynamic rupture propagation on a three-dimensional fault: 2. Traction evolution

and dynamic parameters. *J. Geophys. Res., 111*, B05304. doi:10.1029/2005JB003864.

Boatwright & M. Cocco (1996). Frictional constraints on crustal faulting. *J. Geophys. Res., 101*(B6), 13895–13909. doi: 10.1029/96JB00405.

Boncio, P., Lavecchia, G., & Pace, B. (2004a). Defining a model of 3D seismogenic sources for Seismic Hazard Assessment applications: the case of central Apennines (Italy). *Journal of Seismology, 8*(3), 407-425.

Boncio, P., Lavecchia, G., Milana, G., & Rozzi, B. (2004b). Seismogenesis in Central Apennines, Italy: an integrated analysis of minor earthquake sequences and structural data in the Amatrice-Campotosto area. *Annals of Geophysics*, *47*(6).

Butler, R. W., Tavarnelli, E., & Grasso, M. (2006). Structural inheritance in mountain belts: an Alpine–Apennine perspective. *Journal of Structural Geology, 28*(11), 1893-1908.

Calamita, F., Cello, G., Centamore, E., Deiana, G., Micarelli, A., Paltrinieri, W., & Ridolfi, M. (1991). Stile deformativo e cronologia della deformazione lungo tre sezioni bilanciate dall'Appennino umbro-marchigiano alla costa adriatica. *Studi Geol. Camerti*, *1*(1991), 295-314.

Calamita, F., Pace, P., & Satolli, S. (2012a). Coexistence of fault-propagation and fault-bend folding in curve-shaped foreland fold-and-thrust belts: examples from the Northern Apennines (Italy). *Terra Nova*, *24*(5), 396-406.

Calamita, F., Satolli, S., & Turtù, A. (2012b). Analysis of thrust shear zones in curve-shaped belts: Deformation mode and timing of the Olevano-Antrodoco-Sibillini thrust (Central/Northern Apennines of Italy). *Journal of Structural Geology*, *44*, 179-187.

Carminati, E., & Doglioni, C. (2012). Alps vs. Apennines: the paradigm of a tectonically asymmetric Earth. *Earth-Science Reviews*, *112*(1), 67-96.

Castellarin, A., Colacicchi, R., & Praturlon, A. (1978). Fasi distensive, trascorrenze e sovrascorrimenti lungo la Linea Ancona-Anzio, dal Lias Medio al Pliocene. *Geologica Romana*, 27, 161-189.

Cavinato, G. P., & De Celles, P. G. (1999). Extensional basins in the tectonically bimodal central Apennines fold-thrust belt, Italy: response to corner flow above a subducting slab in retrograde motion. *Geology, 27*(10), 955-958.

Centamore, E., Adamoli L., Berti D., Bigi S., Casnedi R., Cantalamessa G., ... Potetti M. (1992). Carta geologica dei bacini della Laga e del Cellino e dei rilievi carbonatici

circostanti, in Studi Geologici Camerti, Vol. Spec., Università degli Studi, Dipartimento di Scienze della Terra, SELCA, Firenze.

Centamore, E., Rossi, D., & Tavarnelli, E. (2009). Geometry and kinematics of Triassic-to-Recent structures in the Northern-Central Apennines: a review and an original working hypothesis. *Bollettino della Società Geologica Italiana*, *128*(2), 419-432.

Cheloni, D., De Novellis, V., Albano, M., Antonioli, A., Anzidei, M., Atzori, S., … Doglioni C. (2017). Geodetic model of the 2016 Central Italy earthquake sequence inferred from InSAR and GPS data. Geophys. *Res. Lett. 44*, 6778–6787. doi: 10.1002/2017GL073580.   Chiarabba, C., Jovane, L., & DiStefano, R. (2005). A new view of Italian seismicity using 20 years of instrumental recordings. *Tectonophysics*, *395*(3), 251-268.

Chiaraluce, L., W. L. Ellsworth, C. Chiarabba, & M. Cocco (2003). Imaging the complexity of an active normal fault system: The 1997 Colfiorito (central Italy) case study. *J. Geophys. Res. 108*(B6). doi: 10.1029/2002JB002166.

Chiaraluce, L., Barchi, M., Collettini, C., Mirabella, F., & Pucci, S. (2005). Connecting seismically active normal faults with Quaternary geological structures in a complex extensional environment: The Colfiorito 1997 case history (northern Apennines, Italy). *Tectonics*, *24*(1).

Chiaraluce, L., R. Di Stefano, E. Tinti, L. Scognamiglio, M. Michele, E. Casarotti, ... S. Marzorati (2017). The 2016 Central Italy Seismic Sequence: A First Look at the Mainshocks, Aftershocks, and Source Models. *Seismol. Res. Lett., 88*(3). doi: 10.1785/0220160221.

Ciarapica, G., & Passeri, L. (2002). The palaeogeographic duplicity of the Apennines. *Bollettino della Società Geologica Italiana, 121*(1), 67-75.

Cirella, A., A. Piatanesi, E. Tinti, M. Chini & M. Cocco (2012). Complexity of the rupture process during the 2009 L'Aquila, Italy, earthquake. *Geophys. J.Int., 190*, 607-621. doi: 10.1111/j.1365-246X.2012.05505.x.

Coltorti, M., & Farabollini, P. (1995). Quaternary evolution of the Castelluccio di Norcia basin (Umbro-Marchean Apennines, central Italy). *Il Quaternario*, *8*(1), 149-166.

Cultrera, G., D'Alema, E., Amoroso, S., Angioni, B., Bordoni, P., Cantore L., … Vassallo M. (2016). Site effect studies following the 2016 Mw 6.0 Amatrice earthquake (Italy): the Emersito Task Force activities. *Annals of Geophysics, 59*, Fast Track 5.

http://doi.org/10.4401/ag-7189.

D'Agostino, N., Mantenuto, S., D'Anastasio, E., Avallone, A., Barchi, M., Collettini, C., Radicioni, F., Stoppini, A., & Fastellini, G. (2009). Contemporary crustal extension in the Umbria–Marche Apennines from regional CGPS networks and comparison between geodetic and seismic deformation. *Tectonophysics, 476*(1), 3-12.

D'Agostino, N., Jackson, J. A., Dramis, F., & Funiciello, R. (2001). Interactions between mantle upwelling, drainage evolution and active normal faulting: an example from the central Apennines (Italy). *Geophysical Journal International*, *147*(2), 475-497.

Di Domenica, A., Bonini, L., Calamita, F., Toscani, G., Galuppo, C., & Seno, S. (2014). Analogue modeling of positive inversion tectonics along differently oriented pre-thrusting normal faults: An application to the Central-Northern Apennines of Italy. *Geological Society of America Bulletin*, *126*(7-8), 943-955.

Di Luzio, E., G. Mele, M. M. Tiberti, G. P. Cavinato, & M. Parotto (2009). Moho deepening and shallow upper crustal delamination beneath the central Apennines. *Earth. Planet. Sci. Lett., 280, 112*, doi 10.1016/j.epsl.2008.09.018.

Di Stefano, R., C. Chiarabba, L. Chiaraluce, M. Cocco, P. De Gori, D. Piccinini, & L. Valoroso (2011). Fault zone properties affecting the rupture evolution of the 2009 (Mw 6.1) L'Aquila earthquake (central Italy): Insights from seismic tomography. *Geophys. Res. Lett., 38,* L10310. doi:10.1029/2011GL047365.

Dreger, D. S., L. Gee, P. Lombard, M. H. Murray, & B. Romanowicz (2005). Rapid finite-source analysis and near-fault strong ground motions: Application to the 2003 Mw 6.5 San Simeon and 2004 Mw 6.0 Parkfield earthquakes. *Seismol. Res. Lett., 76*(1), 40–48.

Eberhart-Phillips, D., Haeussler, P.J., Freymueller, J. T., Frankel, A. D., Rubin, C. M., Craw, P., … Wallace, W. K. (2003). The 2002 Denali Fault Earthquake, Alaska: A Large Magnitude, Slip-Partitioned Event. *Science, 300*(5622), 1113-1118. doi: 10.1126/science.1082703.

Emergeo Working Group (2016). The 24 August 2016 Amatrice Earthquake: Coseismic Effects. doi: 10.5281/zenodo.61568.

Fletcher J. M., M. E. Oskin & O. J. Teran, (2016). The role of a keystone fault in triggering the complex El Mayor–Cucapah earthquake rupture. *Nature Geoscience, 9*, 303–307. doi:10.1038/ngeo2660.

Galadini, F., & Galli, P. (2000). Active tectonics in the central Apennines (Italy)–input data for seismic hazard assessment. *Natural Hazards, 22*(3), 225-268.

Galadini, F., & Messina, P. (2001). Plio-Quaternary changes of the normal fault architecture in the central Apennines (Italy). *Geodinamica Acta, 14*(6), 321-344.

Galadini, F., & Galli, P. (2003). Paleoseismology of silent faults in the Central Apennines (Italy): the Mt. Vettore and Laga Mts. faults. *Annals of Geophysics, 46*(5), 815-836.

Galli, P., Galadini, F., & Pantosti, D. (2008). Twenty years of paleoseismology in Italy. *Earth-Science Reviews, 88*(1), 89-117.

Galli, P., E. Peronace, & A. Tertulliani (2016). Rapporto sugli effetti macrosismici del terremoto del 24 Agosto 2016 di Amatrice in scala MCS, Roma, rapporto congiunto DPC, CNR-IGAG, INGV, 15 pp.. doi: 10.5281/zenodo.161323 (in Italian).

Galvani A., M. Anzidei, R. Devoti, A. Esposito, G. Pietrantonio, A.R. Pisani, F. Riguzzi, & E. Serpelloni (2012). The interseismic velocity field of the central Apennines from a dense GPS network. *Ann. Geophys., 55*(4). doi:10.4401/ag-6168.

Gruppo di Lavoro INGV sul Terremoto in centro Italia, (2017). Relazione sullo stato delle conoscenze sulla sequenza sismica in centro Italia 2016-2017 (aggiornamento al 2 febbraio 2017). doi: 10.5281/zenodo.267984.

Gupta, A., & Scholz, C.H. (2000). A model of normal fault interaction based on observations and theory. *J. Struct. Geol., 22*-7, 865-879. doi: 10.1016/S0191-8141(00)00011-0

Hamling, I.J., Hreinsdóttir, S., Clark, K., Elliott, J., Liang, C., Fielding, E., … Stirling, M. (2017). Complex multifault rupture during the 2016 Mw 7.8 Kaikoura earthquake, New Zealand. *Science, 356*(6334). doi: 10.1126/science.aam7194.

Harris R. A., & S. M. Day, (1999). Dynamic 3D simulations of earthquakes on en echelon faults. *Geo. Res. Lett., 26*, 14, 2089-2092.

Hartzell, S. H., & Heaton, T. H. (1983). Inversion of strong ground motion and teleseismic waveform data for the fault rupture history of the 1979 Imperial Valley, California, earthquake. *Bull. Seismol. Soc. Am., 73*, 1553–1583.

Herrmann, R. B., L. Malagnini, & I. Munafò (2011). Regional moment tensor of the 2009 L'Aquila earthquake sequence. *Bull. Seismol. Soc. Am., 101*(3), 975–993.

Huang, M.-H., Dreger, D., Burgmann, R., Yoo, S.-H., & Hashimoto, M. (2013). Joint inversion of seismic and geodetic data for the source of the 2010 March 4, Mw6.3 Jia-Shian, SW Taiwan, earthquake. *Geophys.J.Int., 193*, 1608–1626. doi:10.1093/gji/ggt058.

INGV Working Group "GPS Geodesy, GPS data and data analysis center" (2016). Preliminary co-seismic displacements for the October 26 (M$_W$5.9) and October 30 (M$_W$6.5) central Italy earthquakes from the analysis of GPS stations, Zenodo. doi:10.5281/zenodo.167959.

Johnson K.M., R. Bürgmann & K. Larson, (2006). Frictional Properties on the San Andreas Fault near Parkfield, California, Inferred from Models of Afterslip following the 2004 Earthquake. *Bull. Seismol. Soc. Am., 96*(4B), S321–S338. doi: 10.1785/0120050808.

Kaneko Y., J.P. Avouac & N. Lapusta, (2010). Towards inferring earthquake patterns from geodetic observations of interseismic coupling. *Nature Geoscience, 3*, 363-369. doi:10.1038/ngeo843.

Kaverina, A., Dreger, D., & Price, E. (2002). The combined inversion of seismic and geodetic data for the source process of the 16 October 1999 Mw 7.1 Hector Mine, California, earthquake. *Bull. Seismol. Soc. Am., 92*(4), 1266–1280.

Lavecchia, G. (1985). II sovrascorrimento dei Monti Sibillini: analisi cinematica e strutturale. *Bollettino della Società Geologica Italiana*, *104*, 161-194.

Lavecchia, G., Minelli, G., & Pialli, G. (1988). The Umbria-Marche arcuate fold belt (Italy). *Tectonophysics*, *146*(1), 125-137.

Lavecchia, G., Brozzetti, F., Barchi, M., Menichetti, M., & Keller, J. V. (1994). Seismotectonic zoning in east-central Italy deduced from an analysis of the Neogene to present deformations and related stress fields. *Geological Society of America Bulletin*, *106*(9), 1107-1120.

Lucente, F. P., P. De Gori, L. Margheriti, D. Piccinini, M. Di Bona, C. Chiarabba, & N. P. Agostinetti (2010). Temporal variation of seismic velocity and anisotropy before the 2009 Mw 6.3 L'Aquila earthquake, Italy. *Geology, 38*(11), 1015–1018.

Michelini A., L. Margheriti, M. Cattaneo, G. Cecere, G. D'Anna, A. Delladio, ... G. Selvaggi (2016). The Italian National Seismic Network and the earthquake and tsunami monitoring and surveillance systems. *Adv. Geosci., 43*, 31–38. doi:10.5194/adgeo-43-31-2016.

Miller S.A., Collettini C., Chiaraluce L., Cocco M., Barchi M., & Kaus B. J. P. (2004). Aftershocks driven by a high-pressure CO_2 source at depth. *Nature, 427*, 724-727. doi:10.1038/nature02251.

Montone, P., & Mariucci, M. T. (2016). The new release of the Italian contemporary stress map. *Geophysical Journal International, 205*(3), 1525-1531.

Moretti, M., Pondrelli, S., Margheriti, L., Abruzzese, L., Anselmi, M., Arroucau, P., … Mazza, S. (2016). SISMIKO: emergency network deployment and data sharing for the 2016 central Italy seismic sequence. *Annals of Geophysics, 59,* Fast track 5. doi: http://dx.doi.org/10.4401/ag-7212.

Nicol, A., J. Walsh, K. Berryman, & P. Villarmor, (2006). Interdependence of fault displacement rates and paleoearthquakes in an active rift. *Geology, 34*(10), 865-868. doi: 10.1120/G22335.1.

Noda H., & N. Lapusta, (2013). Stable creeping fault segments can become destructive as a result of dynamic weakening. *Nature, 493*, 518–521. doi:10.1038/nature11703.

Pantosti and the Open EMERGEO Working Group (2017). The surface faulting produced by the 30 October 2016 Mw 6.5 central Italy earthquake: the Open EMERGEO Working Group experience. *Geophysical Research Abstracts, Vol. 19*, EGU General Assembly, Vienna.

Pantosti, D., & G. Valensise (1990). Faulting mechanism and complexity of the November 23, 1980, Campania-Lucania earthquake, inferred from surface observations. *J. Geophys. Res., 95*(B10), 15,319–15,341. doi:10.1029/JB095iB10p15319.

Perfettini, H., Stein, R. S., Simpson, R., & Cocco, M. (1999). Stress transfer by the 1988-1989 M=5.3 and 5.4 Lake Elsman foreshocks to the Loma Prieta fault: Unclamping at the site of peak mainshock slip. *Journal of Geophysical Research*, *104*, 20,169–20,182.

Perfettini, H., Schmittbuhl, J., Rice, J.R., & Cocco, M. (2001). Frictional response induced by time-dependent fluctuations of the normal loading. *Journal of Geophysical Research*, *106*, 13,455-13,472.

Pierantoni, P., Deiana, G., & Galdenzi, S. (2013). Stratigraphic and structural features of the Sibillini mountains (Umbria-Marche Apennines, Italy). *Italian Journal of Geosciences, 132*(3), 497-520.

Pizzi, A., & Galadini, F. (2009). Pre-existing cross-structures and active fault segmentation in the northern-central Apennines (Italy). *Tectonophysics, 476*, 304–319. doi: 10.1016/j.tecto.2009.03.018.

Pizzi, A., A. Di Domenica, F. Gallovič, L. Luzi, R. Puglia (2017). Fault segmentation as constraint to the occurrence of the main shocks of the 2016 Central Italy seismic sequence, *Tectonics*, doi: 10.1002/2017TC004652.

Pucci, S., De Martini, P. M., Civico, R., Villani, F., Nappi, R., Ricci, T., ... Pantosti, D. (2017). Coseismic ruptures of the 24 August 2016, Mw 6.0 Amatrice earthquake (central Italy). *Geophys. Res. Lett., 44*, 2138–2147. doi:10.1002/2016GL071859.

Rice, J. R. (2006). Heating and weakening of faults during earthquake slip. *J. Geophys. Res., 111*, B05311. doi:10.1029/2005JB004006.

Rovida A., Locati M., Camassi R., Lolli B., & Gasperini P. (eds) (2016). CPTI15, the 2015 version of the Parametric Catalogue of Italian Earthquakes. Istituto Nazionale di Geofisica e Vulcanologia. doi:http://doi.org/10.6092/INGV.IT-CPTI15.

Rudnicki, J. W., & J. R. Rice (2006). Effective normal stress alteration due to pore pressure changes induced by dynamic slip propagation on a plane between dissimilar materials. *J. Geophys. Res, 111*(B10), 867–18. doi:10.1029/2006JB004396.

Saikia, C. (1994). Modified frequency-wavenumber algorithm for regional seismograms using Filon's quadrature; modelling of Lg waves in eastern North America. *Geophys. J. Int., 118*, 142–158.

Scognamiglio, L., E. Tinti, & M. Quintiliani (2016). The first month of the 2016 Amatrice seismic sequence: Fast determination of time domain moment tensors and finite fault model analysis of the ML 5.4 aftershock. *Ann. Geophys., 59*. doi: 10.4401/ag-7246.

Scognamiglio, L., E. Tinti, A. Michelini, D.S. Dreger, A. Cirella, M. Cocco, S. Mazza, & A. Piatanesi (2010). Fast Determination of Moment Tensors and Rupture History: What Has Been Learned from the 6 April 2009 L'Aquila Earthquake Sequence. *Seismological Research Letters, 81(6),* 892–90.

Scognamiglio, L., E. Tinti, & A. Michelini (2009). Real-time determination of seismic moment tensor for Italian Region. *Bull. Seismol. Soc. Am., 99(4)*, 2223–2242.

Serpelloni, E., M. Anzidei, P. Baldi, G. Casula, & A. Galvani (2005). Crustal velocity and strain-rate fields in Italy and surrounding regions: New results from the analysis of

permanent and non-permanent GPS networks. *Geophys. J. Int., 161*(3), 861–880.

Speranza, F., & Minelli, L. (2014). Ultra-thick Triassic dolomites control the rupture behavior of the central Apennine seismicity: Evidence from magnetic modeling of the L'Aquila fault zone. *Journal of Geophysical Research: Solid Earth*, *119*(9), 6756-6770.

Tavarnelli, E. (1999). Normal faults in thrust sheets: pre-orogenic extension, post-orogenic extension, or both?. *Journal of Structural Geology*, *21*(8), 1011-1018.

Tinti, E., L. Scognamiglio, A. Michelini, & M. Cocco (2016). Slip heterogeneity and directivity of the ML 6.0, 2016, Amatrice earthquake estimated with rapid finite-fault inversion. *Geophys. Res. Lett., 43*, 10,745–10,752. doi: 10.1002/2016GL071263.

Toda, S., R. S. Stein, V. Sevilgen, & J. Lin (2011). Coulomb 3.3 Graphic-rich deformation and stress-change software for earthquake, tectonic, and volcano research and teaching—User guide: U.S. Geol. Surv. Open File Rep., vol. 63, pp. 2011–1060. [Available at http://pubs. usgs. gov/of/2011/1060/.]

Tondi, E. (2000). Geological analysis and seismic hazard in the central Apennines (Italy). *J. Geodyn., 29*, 517-533.

Valoroso, L., L. Chiaraluce, D. Piccinini, R. Di Stefano, D. Schaff, & F. Waldhauser (2013). Radiography of a normal fault system by 64,000 high-precision earthquake locations: The 2009 L'Aquila (central Italy) case study. *J. Geophys. Res. Solid Earth, 118*, 1156–1176. doi:10.1002/jgrb.50130.

Vezzani, L., Festa, A., & Ghisetti, F. C. (2010). Geology and tectonic evolution of the Central-Southern Apennines, Italy. *Geological Society of America Special Papers, 469*, 1-58.

Wang, C. Y., & Herrmann, R. B. (1980). A numerical study of P-, SV-, and SH-wave generation in a plane layered medium. *Bull. Seismol. Soc. Am., 70*(4), 1015–1036.

Wang, R., Martin, F., & Roth, F. (2003). Computation of deformation induced by earthquakes in multi-layered elastic crust: FORTRAN programs EDGRN/EDCMP. *Comput. Geosci., 29*, 195–207.

Wesnousky, S. G. (2008). Displacement and geometrical characteristics of earthquake surface ruptures: Issues and implications for seismic-hazard analysis and the process of earthquake rupture. *Bulletin of the Seismological Society of America, 98*(4), 1609-1632.

Wilkinson M. W., McCaffrey K.J.W., Jones R.R., Roberts G.P., Holdsworth R.E., Gregory L.C., Walters R.J., Wedmore L., Goodall H. & Iezzi F. (2017). Near-field fault slip

of the 2016 Vettore Mw 6.6 earthquake (Central Italy) measured using low-cost GNSS. *Scientific Reports, 7*(4612). doi: 10.1038/s41598-017-04917-w.
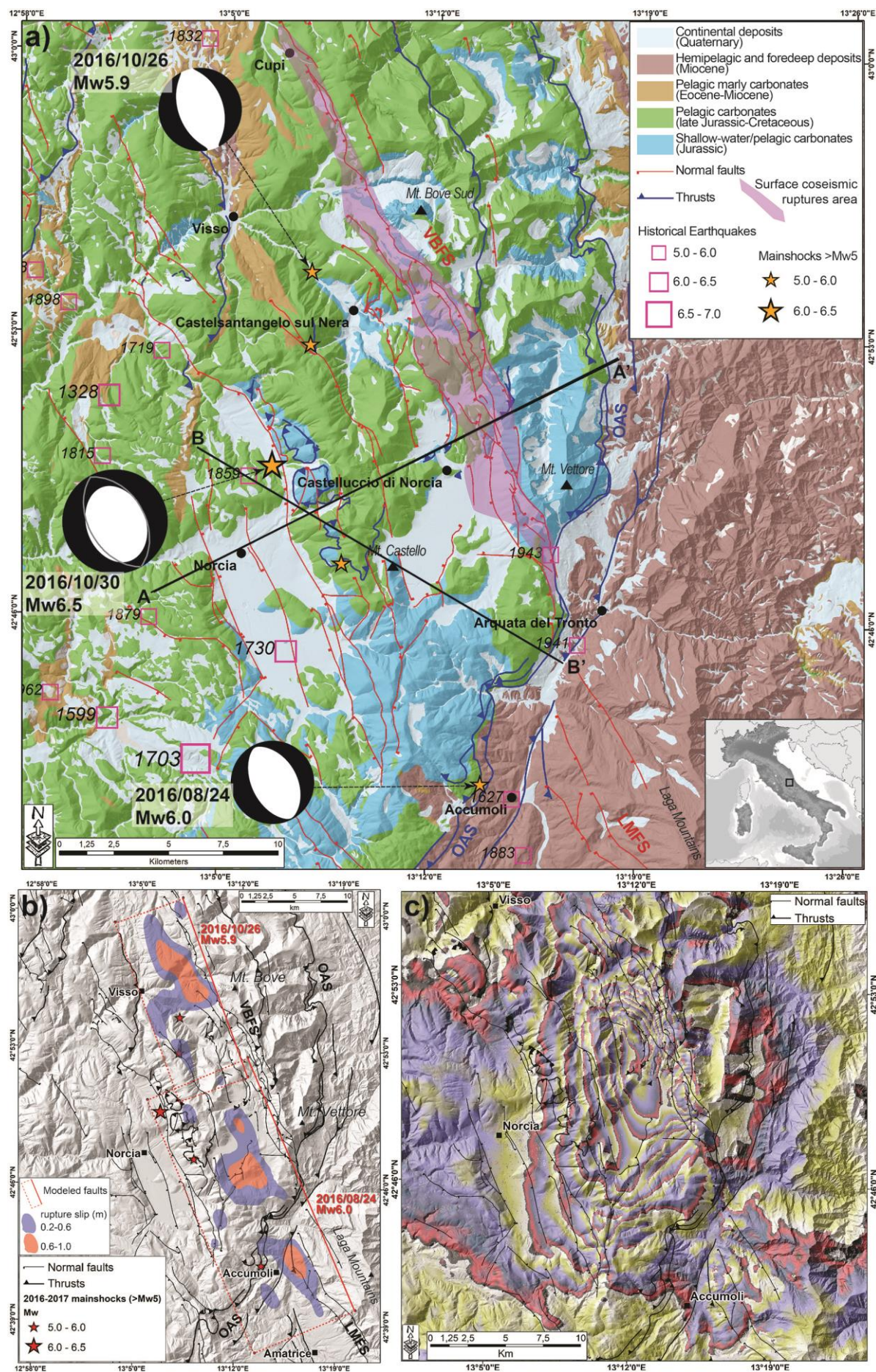
Figure 1: a) Simplified geological map of the study area (compiled from 1:10,000-scale cartography of Regione Umbria and Marche, Centamore et al., 1992 and Pierantoni et al., 2013). The labels VBFS and LMFS indicate the Mt. Vettore-Mt. Bove and Laga Mts. fault systems, respectively, OAS indicates the Olevano-Antrodoco-Sibillini thrust. The shaded pink polygon encloses the area with coseismic surface ruptures following the 2016 mainshocks. The main historical events are reported after Rovida et al. (2016). TDMT solutions for the three mainshocks (http://cnt.rm.ingv.it/) are shown: the solution for the 30th October earthquake shows the low value of the double-couple component (the projected nodal planes on the lower hemisphere are reported in gray). AA' and BB' are the traces of the geological cross sections of figures 9 and 10. b) Map projection of the main slip patches of the kinematic fault models of Amatrice and Visso earthquakes (modified from Tinti et al. 2016 and Chiaraluce et al., 2017, respectively). The red boxes define the surface projection of the inverted faults. c) Far-field coseismic deformation detected by Alos2 interferograms after the 26th, M_W 5.9 and 30th, M_W 6.5 October earthquakes (from descending track interferograms of August 31th and November 9th 2016; Cheloni et al., 2017). Each fringe represents 11.45 cm of displacement along the line of sight.
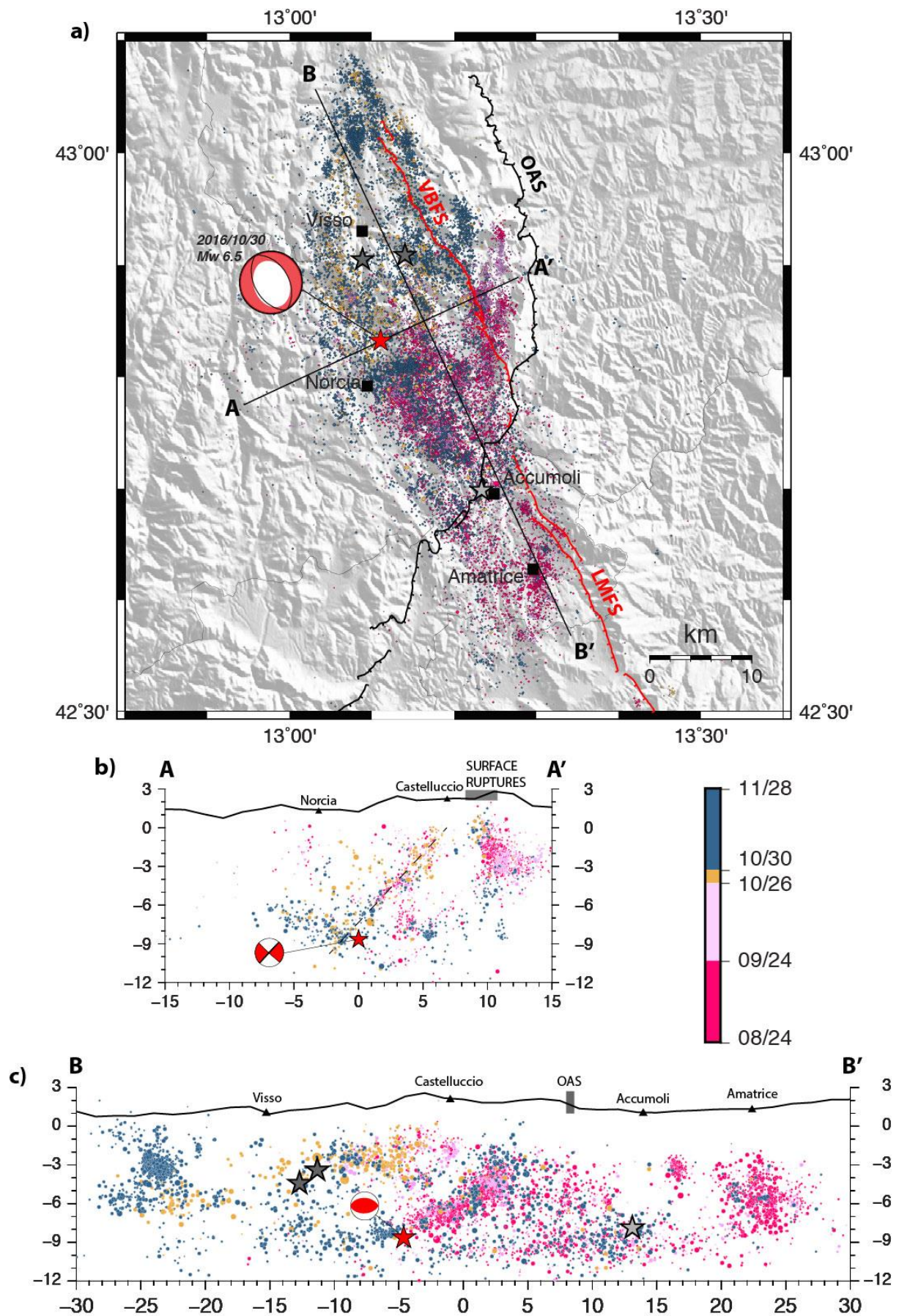
Figure 2: a) Map view of the 25,600 aftershocks relocated by Chiaraluce et al. (2017) occurred between August 24th and November 29th 2016. Color-coded refers to the temporal evolution of the seismicity during the sequence. The light-grey, dark-grey and red stars represent the August 24th, October 26th and 30th 2016 mainshocks, respectively. The 26 October Mw 5.9 earthquake is actually a double event and the two hypocenters are located at ~4 km of distance (Chiaraluce et al. 2017). Red lines are the main normal fault systems of the area (Vettore Mt. - Bove Mt. fault system, VBFS), black lines show the trace of the Olevano-Antrodoco-Sibillini thrust (OAS) (simplified traces, modified from Figure 1). AA' and BB' are the traces of the cross-sections reported in b) and c) where we plot all the events contained within ± 1.5 km of distance from the section. b) The SW-NE (AA') section is 30 km long, it is oriented N65°E (orthogonal to the VBFS) and is centered on the M_W 6.5 hypocenter. The dashed line in figure evidences the alignments of the seismicity on a ~50° SW-dipping structure, matching the main shock hypocenter and coseismic surface rupture retrieved on the VBFS (grey box). The geometry of this fault plane is compatible with the mapped TDMT solution. c) The NW-SE (BB') cross-section (N155°) is longitudinal to the seismogenic volume. This 60 km long section gives a general overview of the whole sequence seismicity and of the activated structures. One of this alignment starts from M_W 6.5 hypocenter and point to the surface expression of the OAS.
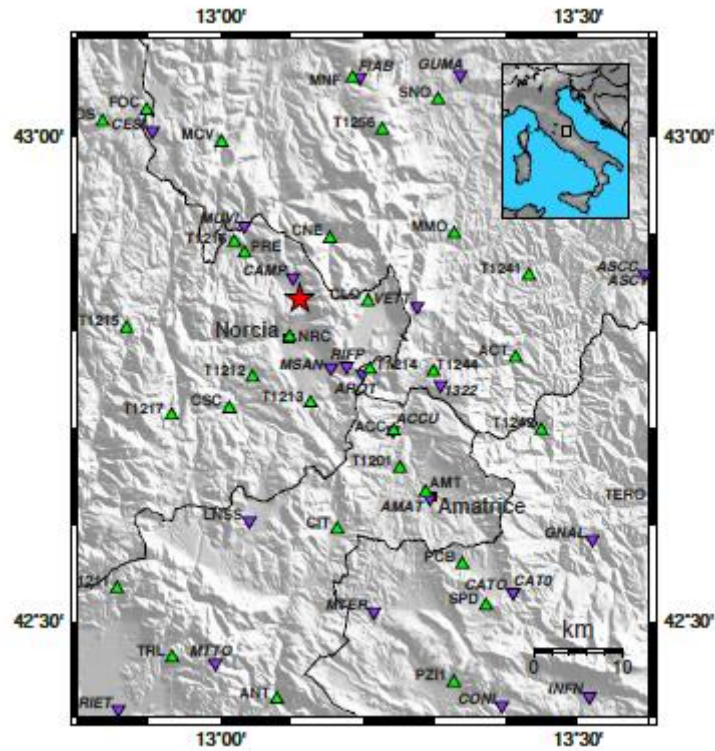
Figure 3: Distribution of the strong motion stations (green triangles) and GPS receivers (violet upside down triangles) used to retrieve the slip model of the October 30th 2016 event. The red star is the M_W 6.5 epicenter location released by INGV.
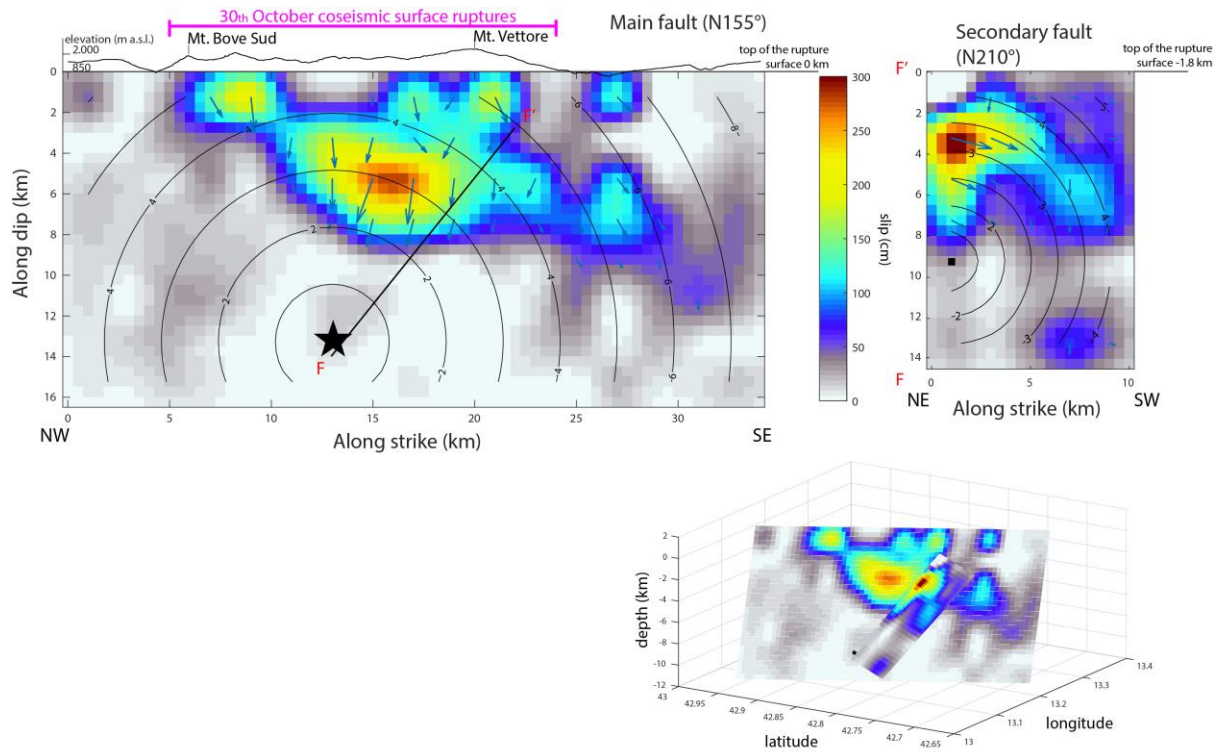
Figure 4: Rupture model imaged in this study by inverting ground velocity time histories and the GPS displacements. Slip amplitudes are expressed in centimeters and rupture times (of the first time window) in seconds, as shown by black contour lines. The blue arrows indicate the slip direction while the FF' black line depicted on the main fault indicates the intersection with the second fault. The 3D plot (bottom) pictures the relative location of the two fault planes. On the top of the main fault the purple bar shows the area interested by coseismic surface rupture due to this earthquake.
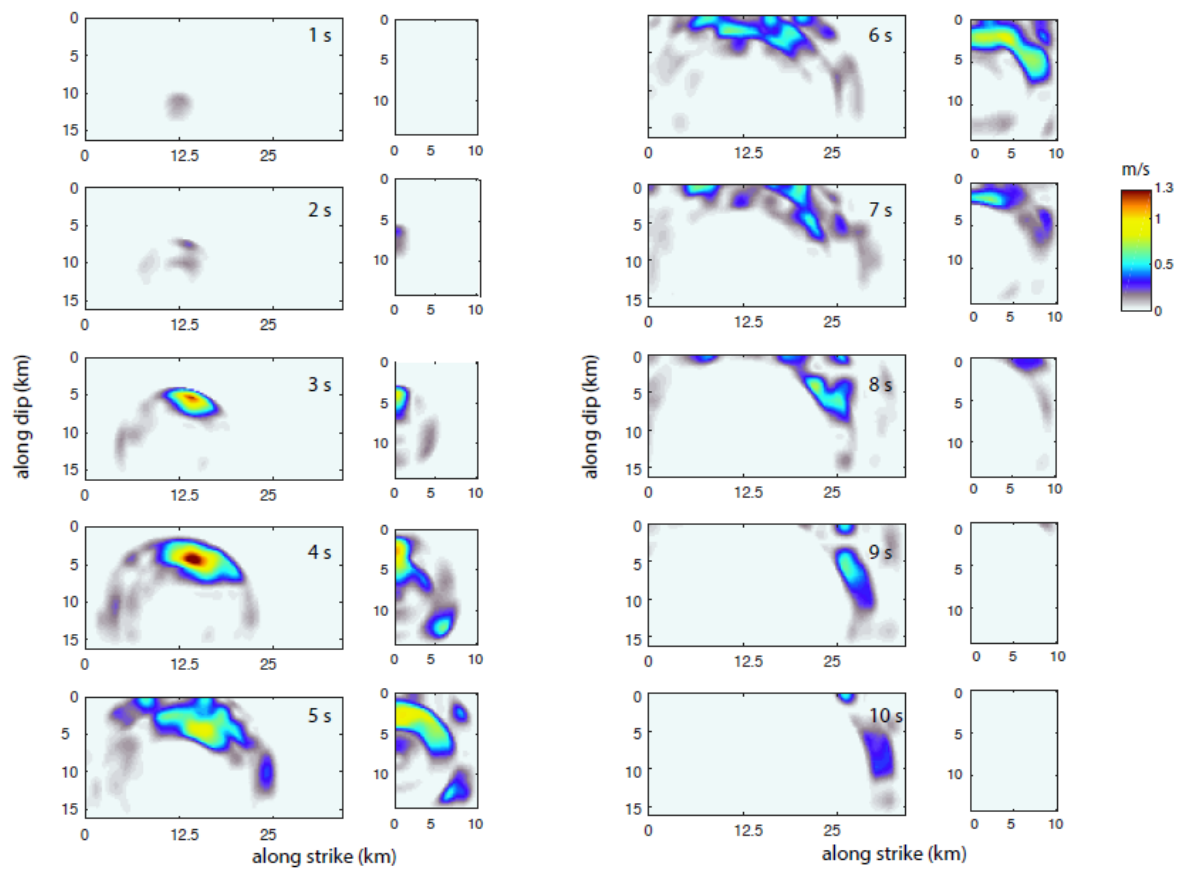
Figure 5: Slip rate distribution mapped every second after the rupture onset on the two fault planes adopted in this study. The snapshots evidence the sudden propagation on the N210° fault segment, nearly one second after nucleation on the N155° segment (2s panel), and the maximum slip reached after 3-4 seconds after the rupture initiation. They also show the rupture propagation on the southeastward portion of the N155° segment, between 5 and 10 seconds after nucleation, in the fault portions that slipped during the August 24th main shock.
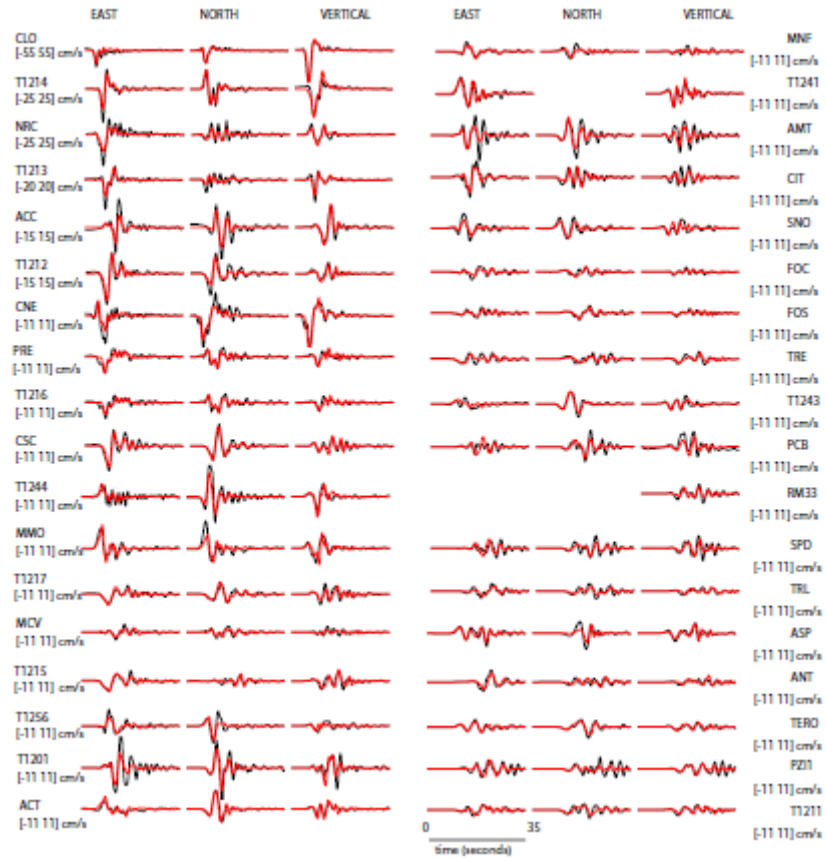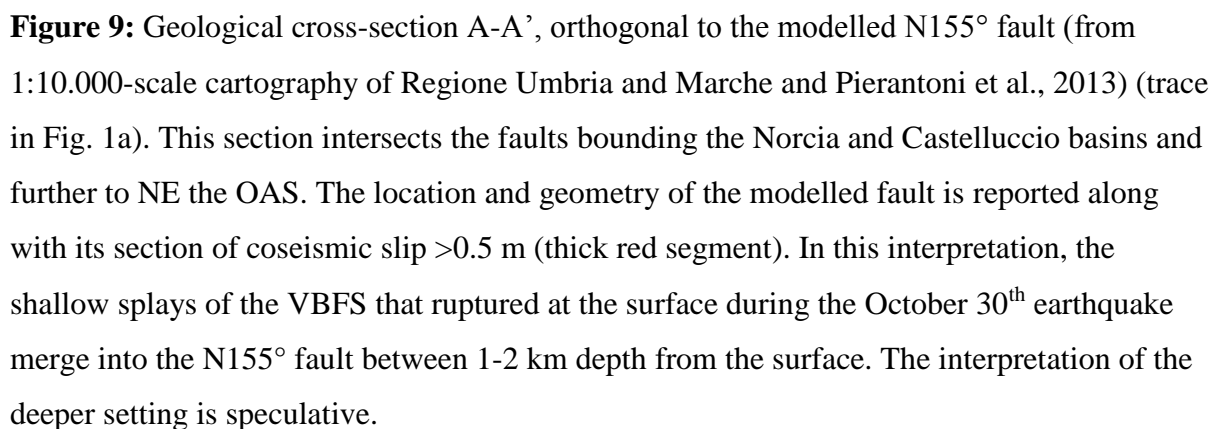
Figure 6: Fit to the velocity converted strong motion data: synthetic (red lines) and recorded velocity ground motions (black lines) both filtered between 0.02 and 0.5 Hz. Numbers in brackets represent the amplitude range of the plot in cm/s for each station.
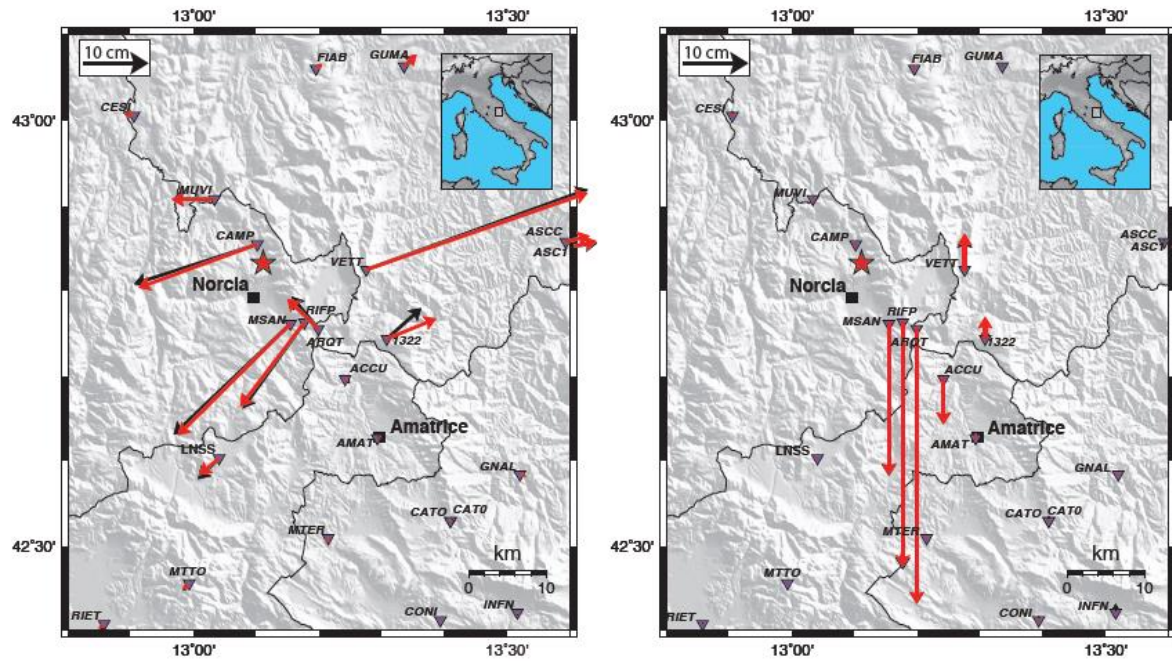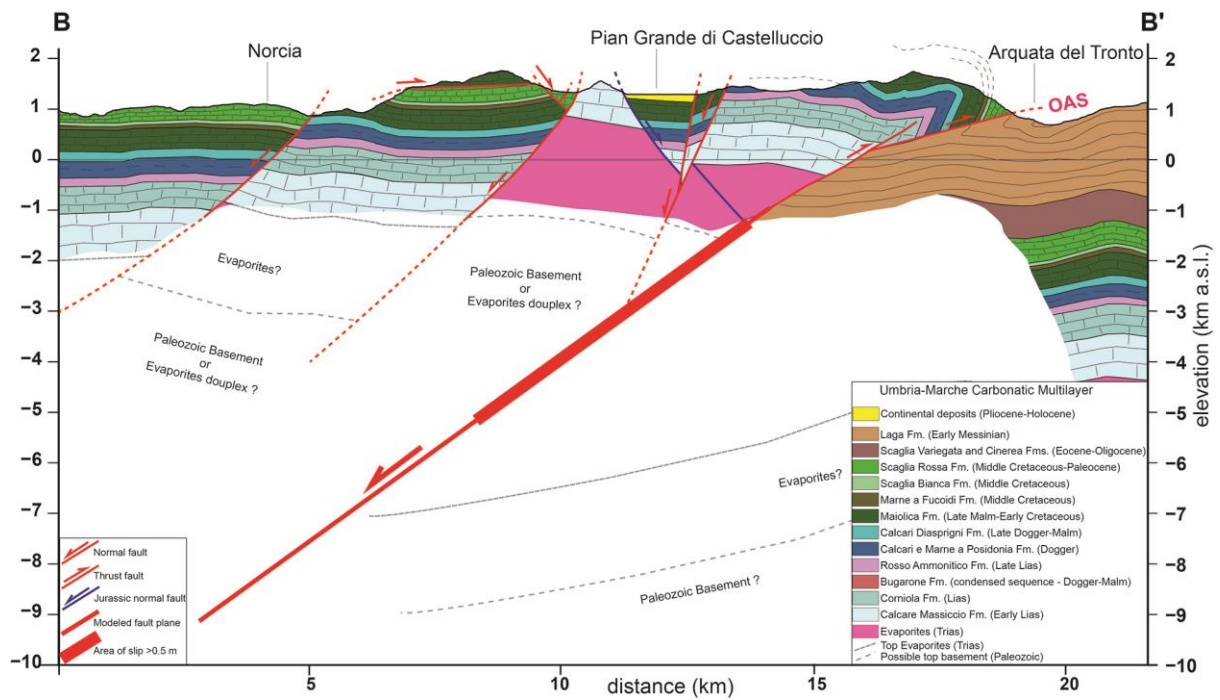
Figure 7**:** Fit to the GPS data: Comparison between observed (black) and synthetic (red) horizontal displacement (left panel), and vertical displacement (right panel). The red star is the epicenter location released by INGV.
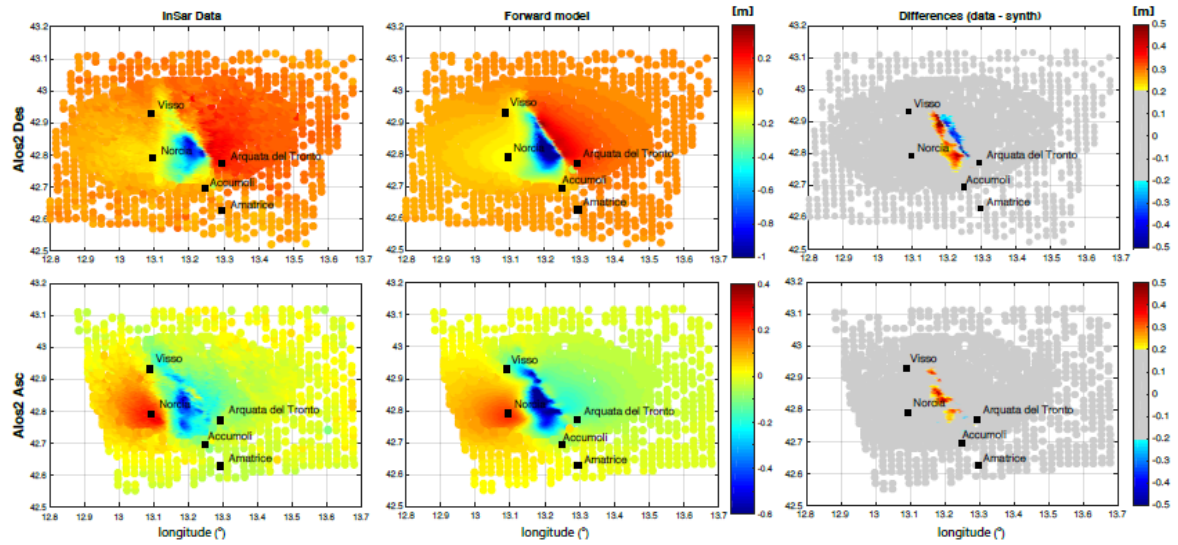
Figure 8: Comparison between observed and synthetic interferograms. Data displacements field are from the unwrapped Alos2 interferograms (left panels) [Cheloni et al., 2017] while synthetic field is obtained with the kinematic rupture model shown in Figure 4 summed to the October 26th source model as imaged by Chiaraluce et al. [2017] (mid-panels). Displacements are plotted along the descending (top) and ascending (bottom) Alos2 LoS. Right panels show the difference between data and synthetics. Residuals lower than ± 20 cm are plotted in grey.

Figure 9: Geological cross-section A-A', orthogonal to the modelled N155° fault (from 1:10.000-scale cartography of Regione Umbria and Marche and Pierantoni et al., 2013) (trace in Fig. 1a). This section intersects the faults bounding the Norcia and Castelluccio basins and further to NE the OAS. The location and geometry of the modelled fault is reported along with its section of coseismic slip >0.5 m (thick red segment). In this interpretation, the shallow splays of the VBFS that ruptured at the surface during the October 30th earthquake merge into the N155° fault between 1-2 km depth from the surface. The interpretation of the deeper setting is speculative.

Figure 10: Geological cross-section B-B', orthogonal to the modelled N210° fault and to the OAS (from 1:10.000-scale cartography of Regione Umbria and Marche and Pierantoni et al., 2013) (trace in Fig. 1a). The location and geometry of the modelled fault is reported along with its section of coseismic slip >0.5 m (hick red segment). In this interpretation, a deep blind ramp of the OAS thrust was re-activated with reversal slip motion during the October 30th earthquake. The interpretation of the deeper setting is speculative.
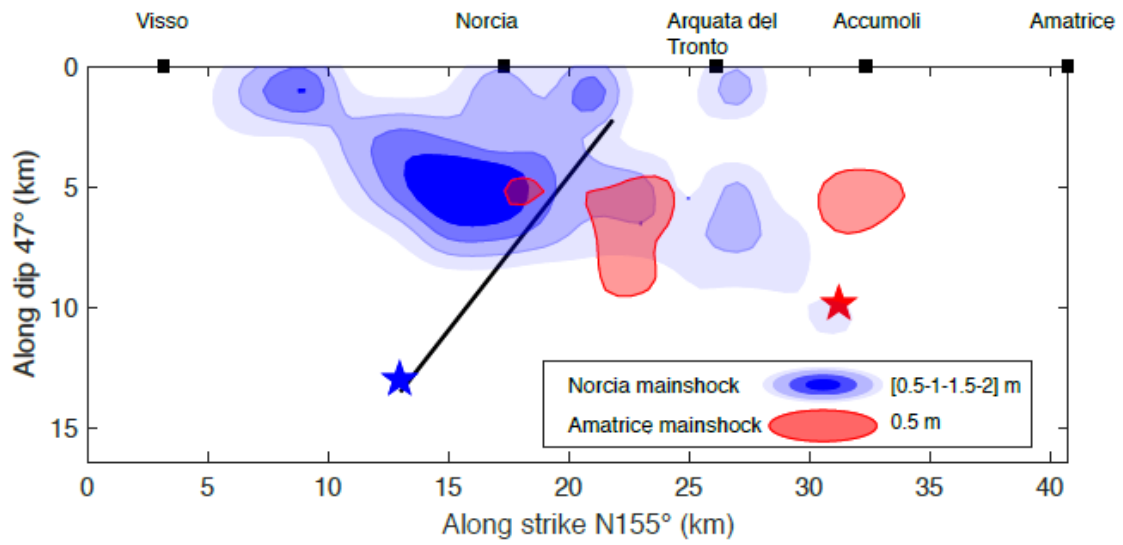
Figure 11: Comparison between the slip distributions imaged on the VBFS fault during the August 24th (red contours; Tinti et al., 2016) and the October 30th 2016 main shocks (blue contours; this study) projected on the same fault striking 155° and dipping 47°. Red and blue stars are the two mainshocks hypocentral locations.

Table 1: Values of the kinematic parameters for the presented model.

	RISE TIME (s)	RUPTURE VELOCITY (km/s)	NUCLEATION POINT	DELAY TIME (s)	M_0 (Nm)	AVERAGE SLIP ON FAULT (m)	AVERAGE SLIP ON AREA WITH SLIP > 20% OF PEAK (m)	MAXIMUM SLIP (m)
FAULT N155°	1.2	2.8	lat: 42.84°N lon: 13.11°E depth: 9.52 km	0	$5.9e^{+18}$	0.4	1.2	2.8
FAULT N210°	1.2	2.7	lat: 42.82°N lon: 13.15°E depth: 7.13 km	1	$2.9e^{+18}$	0.6	1.2	3.1